Separating cognitive and motor processes in the behaving mouse

Munib A. Hasnain[1,3*], Jaclyn E. Birnbaum[2,3*], Juan Luis Ugarte Nunez[1], Emma K. Hartman[1], Chandramouli Chandrasekaran[4,5,6], Michael N. Economo[1,3,6#]

* These authors contributed equally. Order determined via coin flip.

Corresponding author

Email: mne@bu.edu

[1] *Department of Biomedical Engineering, Boston University, Boston, MA*

[2] *Graduate Program for Neuroscience, Boston University, Boston, MA*

[3] *Center for Neurophotonics, Boston University, Boston, MA*

[4] *Department of Psychological and Brain Sciences, Boston University, Boston, MA*

[5] *Department of Neurobiology & Anatomy, Boston University, Boston, MA*

[6] *Center for Systems Neuroscience, Boston University, Boston, MA*

Abstract

The cognitive processes supporting complex animal behavior are closely associated with ubiquitous movements responsible for our posture, facial expressions, ability to actively sample our sensory environments, and other critical processes. These movements are strongly related to neural activity across much of the brain and are often highly correlated with ongoing cognitive processes, making it challenging to dissociate the neural dynamics that support cognitive processes from those supporting related movements. In such cases, a critical issue is whether cognitive processes are separable from related movements, or if they are driven by common neural mechanisms. Here, we demonstrate how the separability of cognitive and motor processes can be assessed, and, when separable, how the neural dynamics associated with each component can be isolated. We establish a novel two-context behavioral task in mice that involves multiple cognitive processes and show that commonly observed dynamics taken to support cognitive processes are strongly contaminated by movements. When cognitive and motor components are isolated using a novel approach for subspace decomposition, we find that they exhibit distinct dynamical trajectories. Further, properly accounting for movement revealed that largely separate populations of cells encode cognitive and motor variables, in contrast to the 'mixed selectivity' often reported. Accurately isolating the dynamics associated with particular cognitive and motor processes will be essential for developing conceptual and computational models of neural circuit function and evaluating the function of the cell types of which neural circuits are composed.

Introduction

Goal-directed behavior follows from an interplay between cognitive and motor processes in the mammalian brain. For example, while dribbling down the court, a basketball player must track the players around them, decide which play to run, plan their next move, execute fast and accurate movements, and flexibly adapt those movements according to the actions of other players. The neural representations of these cognitive and motor processes are often distributed across many of the same brain areas[1–6] and engaged concurrently[7–9]. For these reasons, disentangling the neural signatures of specific cognitive and motor processes is challenging.

Many behavioral tasks are designed with this issue in mind, aiming to isolate constituent neural processes by separating them into discrete temporal epochs. For example, in sensory-guided decision-making tasks, subjects are often trained to withhold responses while stimuli are presented so that perceptual decision making is isolated in time from associated actions. Analogous paradigms have been developed to uncover the neural underpinnings of working memory[10–12], motor planning[13,14], contextual encoding[15,16], reward prediction[17,18], and other cognitive processes[19–22].

These paradigms often rely on the assumption that experimental subjects withhold motor output during task epochs in which instructed responses are absent. However, uninstructed movements not required for task completion – such as changes in posture, facial expressions, and gaze – are commonly observed in rodents, humans, and non-human primates during learned behavioral tasks[23–29]. Importantly, uninstructed movements explain much of the variance observed in brain-wide neural activity[27,30–32] and can be strongly correlated with task variables[12,28,33–38].

These observations imply a serious challenge for experimental studies addressing a wide-ranging set of cognitive processes. If uninstructed movements are correlated with a latent cognitive variable of interest – a stimulus perceived, a decision made, a memory stored, or a motor plan formed – then the neural dynamics leading to, or resulting from, uninstructed movements can be easily misconstrued as responsible for that cognitive process. One common approach to isolate putative cognitive dynamics is to track and 'regress out' movements[24,30,39–44], but this approach assumes that cognitive and motor processes are separable - that is, driven by independent neural dynamics. However, some cognitive processes may be inherently embodied such that their associated neural dynamics are linked to overt movement[45,46]. Regressing out neural dynamics associated with embodied movements would lead to the inadvertent removal of the precise dynamics one wishes to study. Whether cognitive and motor dynamics are separable remains an open question and likely depends on the brain area, behavior, and cognitive process of interest. Effective methods both for evaluating separability within specific experimental paradigms and for effectively dissociating cognitive and motor dynamics, when separable, are lacking.

Here, we address the separability of dynamics associated with cognitive processes and correlated movements. We developed a behavioral paradigm in which mice perform sensory-guided movements involving multiple cognitive signals in which they often exhibit idiosyncratic, task-correlated uninstructed movements. We build upon work demonstrating how different neural processes can be multiplexed in a single brain region[39,40,47–50] to develop a novel method for assessing whether cognitive dynamics can be separated from those associated with movements – and for isolating each component, when they are separable. This approach is simple to adopt and does not require tracking or segmentation of body parts. It also does not require an explicit choice of models relating neural dynamics to movement, avoiding common assumptions of linearity. We find that some cognitive signals are separable from dynamics associated with co-occurring movements while others are largely inseparable. When dynamics are separable, examining the component of neural dynamics unrelated to movement revealed trajectories that differed in notable ways from estimates of the same dynamics when corrupted by uninstructed movements. Strikingly, we found that cognitive and motor dynamics were largely encoded by separate populations of cells when uninstructed movements were accounted for. Together, these results highlight the importance of critical consideration of the relationship between cognition and movement to better understand the neural dynamics supporting complex processes and how they map onto the myriad cell types comprising neural circuits.

Results
Task-switching behavioral paradigm

We first designed a behavioral paradigm associated with multiple cognitive processes. In this paradigm, head-fixed mice performed two directional licking tasks that alternated block-wise within each behavioral session. These tasks varied in their cognitive demands but required the same instructed motor output.

85   This paradigm employed an established delayed-response task (DR) in which motor planning is temporally
86   dissociated from movement execution[14] (**Fig. 1a**). In the DR task, an auditory stimulus indicated the location of a
87   reward. After a brief delay epoch with no auditory stimuli, a separate auditory 'go cue' instructed the mouse to
88   move. If the mouse performed a directional tongue movement to the correct target, a water reward was delivered.
89   In separate blocks of trials, mice performed a water-cued (WC) task in which all auditory stimuli were omitted.
90   Instead, a drop of water was presented at a random point in time at a randomly selected reward port. Animals
91   consumed water upon its presentation. Mice received no explicit cues signaling DR and WC blocks. The DR task
92   required a perceptual decision that guides the planning of a subsequent motor action. In the WC task, uncertainty
93   in the timing and location of reward prevented formation of a motor plan prior to reward presentation, and instead,
94   mice detected reward availability using olfactory and/or vibrissal cues[51]. This structure required animals to maintain
95   an internal representation of the current block identity (context) to maintain high task performance.

96   We examined uninstructed movements in this behavioral paradigm using high-speed video. We tracked movement
97   of the tongue, jaw, nose, and paws[52] and calculated instantaneous motion energy to quantify movement in a feature-
98   agnostic manner[31] (**Fig. 1d-f**). We found that mice performed uninstructed movements that varied in their identity
99   and timing across both trials and contexts (**Fig. 1e** and **Supplementary Movie 1**).

100 Prior work has established the necessity of the antero-lateral motor cortex (ALM) and tongue-jaw motor cortex
101 (tjM1) for the planning and execution of tongue movements[14,53–56]. To assess cortical involvement in the initiation
102 of instructed movements (directional licking) in both behavioral tasks, we used optogenetic photoinactivation to
103 inhibit the ALM and tjM1 at the go cue (DR) or water presentation (WC) bilaterally in VGAT-ChR2-EYFP mice
104 (10 sessions, 4 mice). Simultaneous photoinactivation of both regions at the go cue (DR task) or water drop (WC
105 task) impaired the initiation of movement in both contexts (**Fig. 1b,c**; DR trials: $41 \pm 20\%$ reduction, mean $\pm$ s.d.,
106 $p = 1 \times 10^{-4}$; DR left trials: $58 \pm 19\%$, $p = 4 \times 10^{-6}$, DR right trials: $30 \pm 28\%$, $p = 7 \times 10^{-3}$; All WC trials: $15 \pm 20\%$, p
107 $= 0.04$; WC left trials: $23 \pm 24\%$, $p = 0.01$, WC right trials: $18 \pm 23\%$, $p = 0.03$; paired t-tests; **EDFig. 1c,d**). To
108 assess cortical involvement in the expression of uninstructed movements, and whether these movements might be
109 controlled by ALM or tjM1 preferentially, we bilaterally silenced the ALM and tjM1 during the delay epoch of DR
110 trials individually (ALM: 15 sessions, tjM1: 9 sessions, 4 mice). Uninstructed movements were suppressed by
111 photoinactivation of either area (**EDFig. 1b**; ALM: ; $53 \pm 31\%$ reduction, mean $\pm$ s.d., $p = 3 \times 10^{-4}$; tjM1: $62 \pm 24\%$
112 reduction, $p = 2 \times 10^{-3}$, paired t-test) and more strongly suppressed by concurrent photoinactivation of both areas
113 (**Fig. 1g-h**; 29 sessions, 4 mice; $73 \pm 35\%$ reduction, mean $\pm$ s.d., $p = 7 \times 10^{-9}$, paired t-test), similar to previous
114 observations[34] (but see ref[57]). In the DR task, delay photoinactivation of both areas led to a significant decrease in
115 overall performance (**Fig. 1i**; $22\% \pm 14\%$ reduction, mean $\pm$ s.d., $p = 2 \times 10^{-6}$ paired t-test; **EDFig. 1b**) as expected
116 from the disruption of choice/planning dynamics[14], often leading to animals responding consistently to a preferred
117 side rather than in a manner commensurate with the sensory cue. These results indicate that both the ALM and
118 tjM1 are involved in the generation of uninstructed movements and the planning and execution of instructed
119 directional tongue movements in the two-context paradigm.

120 **Neural dynamics related to task variables**
121 While movement- and task-related information is encoded in both the ALM and tjM1 in the DR task[53,58] and other
122 directional licking tasks[55], task variables are more strongly represented in the ALM[55,56,59] and so we focused our
123 subsequent analyses there. We recorded activity extracellularly in the ALM with high-density silicon probes during
124 the two-context paradigm to track dynamics associated with planning, context, and the execution of movements
125 (**Fig. 2**; two-context paradigm: 12 sessions, 6 mice, 522 units including 214 well-isolated single units; an additional
126 3 mice were trained only on the DR task totaling 25 sessions, 9 mice, 1651 units including 483 well-isolated single
127 units included in analyses of the DR task only; see **EDFig. 2a** for per-session statistics). In the DR task, we found
128 that choice selectivity (right vs. left DR trials) was widespread across all task epochs as expected (sample: 36%;
129 delay: 42%; response: 58% of 483 single units, 25 sessions, 9 mice, 483 single units; see **Methods**). Individual units
130 showed a variety of activity patterns across trial types, including delay epoch preparatory activity preceding
131 instructed movements, often taken to be a signature of motor planning[54,60] (**Fig. 2b left**). Individual units were also
132 selective for behavioral context during all task epochs, including during the inter-trial interval (ITI) (39% of single
133 units, 12 sessions, 6 mice, 214 single units; see **Methods**), suggesting persistent coding of context (**Fig. 2b**, *right*).
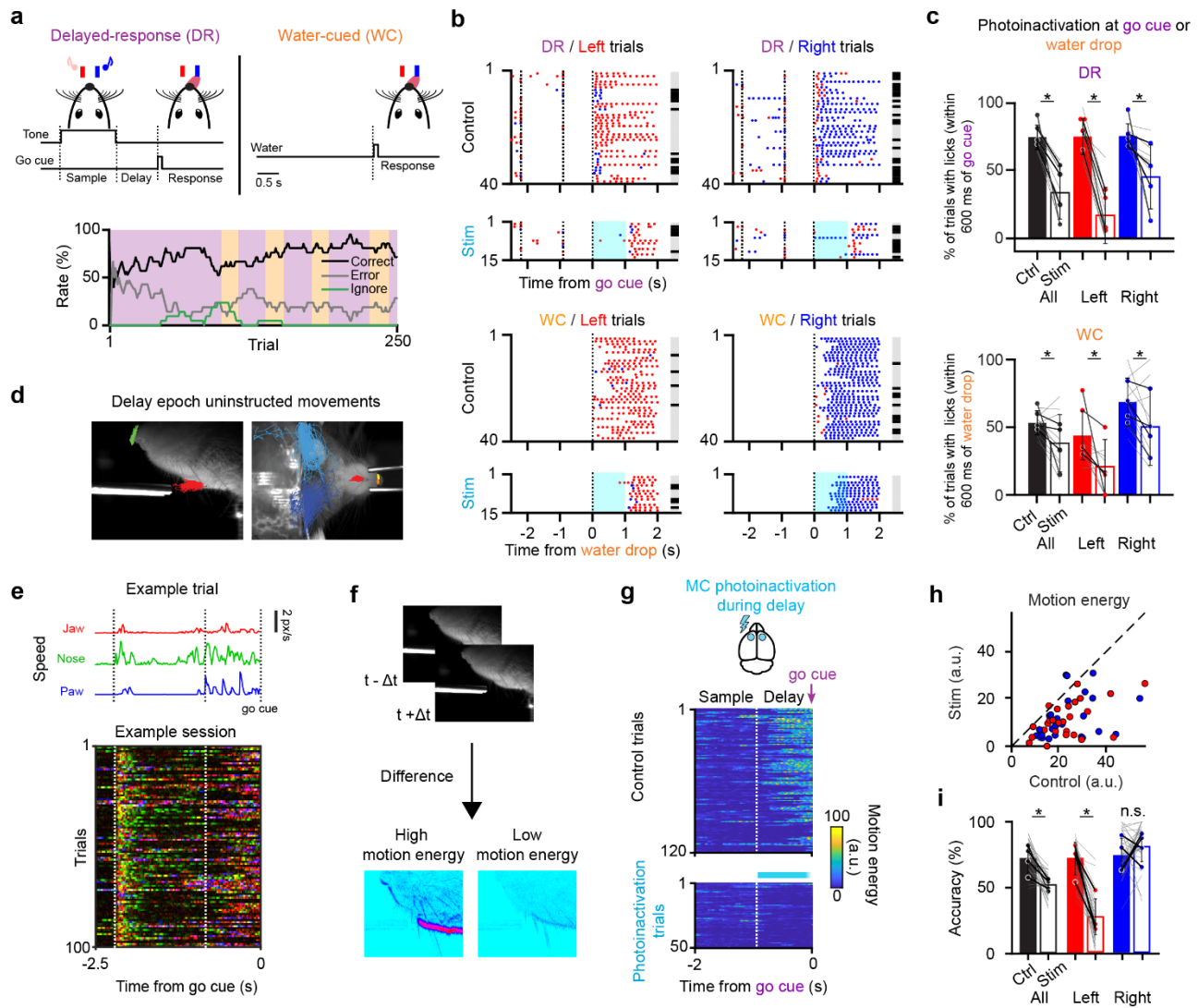
Figure 1 – Cortical dependence and uninstructed movements during a two-context task. a. *Top*, Schematic of the two-context task. In delayed-response (DR) trials, an auditory stimulus was presented during the sample epoch (1.3 s) instructing mice to lick for reward to the right (white noise) or left (8 kHz tone). Mice were trained to withhold their response during a delay epoch (0.9 s) and initiated their response following an auditory go cue. In WC trials, mice were presented with a water reward at a random port at random inter-reward intervals. The WC task was introduced once mice became experts in the DR task. *Bottom*, 20-trial trailing average of correct, error, and ignore rates for an example session. **b.** Performance for an example session separated by trial type (left vs. right), control vs. photoinactivation trials, and by context. Photoinactivation (1 s) was initiated at the go cue. Blue dots indicate right licks and red dots indicate left licks. Grey bars, correct trials; black bars, error trials. **c.** Percent of trials with correct licks within 600 ms of the go cue on photoinactivation trials. Colored points represent mean values across animals (*n* = 4, individual animals connected by dark lines). Light gray lines denote individual sessions (*n* = 10). Bars are across-session means. Asterisks denote significant differences ($p < 0.05$) between control and photoinactivation trials (All DR trials: $p = 0.0001$; DR left trials: $p = 4.5e-06$; DR right trials: $p = 0.0074$; All WC trials: $p = 0.0371$; WC left trials: $p = 0.0134$; WC right trials: $p = 0.0316$, paired *t*-test). Error bars denote standard deviation across sessions. **d.** Behavior was tracked with high-speed video from side (*left*) and bottom (*right*) views. Trajectories of delay epoch uninstructed movements from an example session overlayed. **e.** Uninstructed movements are highly variable across trials and across time. *Top*, jaw, nose, and paw speed for an example trial. *Bottom*, feature overlay for a subset of trials in an example session. At each time bin, *t*, an [r, g, b] color value was encoded as [jaw$_t$, nose$_t$, paw$_t$]. **f.** Schematic of motion energy calculation. Example frames depicting high and low motion energy are shown. **g-i.** Bilateral motor cortex photoinactivation during the delay epoch. **g.** Motion energy on control (*top*) and photoinactivation (*bottom*) trials for an example session. On photoinactivation trials, light was delivered for 0.8 seconds beginning at the start of the delay epoch. **h.** Average delay epoch motion energy on single sessions for control and photoinactivation trials (*n* = 29 sessions, 4 mice). Red points indicate left trials and blue points indicate right trials for a single session. **i.** Performance for control and delay epoch photoinactivation trials. Mice often defaulted to a right choice following delay epoch photoinactivation. Asterisks denote significant differences ($p < 0.05$) between control and photoinactivation trials (n=29 sessions, 4 mice). Black lines and points indicate averages across sessions for individual animals and light grey lines indicate sessions.

158 We next sought to understand how the selectivity patterns observed in individual cells were encoded at the
159 population level. We examined neural activity in state space, in which the firing rate of each unit represents one
160 dimension. We defined one-dimensional coding directions (CD) within the high-dimensional state space that best
161 encoded task variables[54,61–63] (**Fig. 2c**). We first examined putative neural correlates of three cognitive processes –
162 choice, urgency, and contextual encoding.

163 We defined a coding direction for left-right trial type, CD_{choice}, as the direction in state space that best differentiates
164 activity on left versus right trials during the delay epoch of DR trials. Projections along CD_{choice} revealed that choice
165 selectivity in the ALM emerges early in the sample epoch and continues to grow throughout the delay epoch before
166 decaying at the onset of the response epoch (**Fig. 2d**). Choice could be reliably decoded from projections along
167 CD_{choice} across sessions (**EDFig. 2c**; AUC: 0.86 ± 0.11 mean $\pm$ s.d.). Such preparatory activity is predictive of
168 animals' upcoming instructed responses[13,54,58,61,64,65] and has been taken to represent a neural correlate of a motor
169 plan[54,60] or choice[32,62,66]. We next defined CD_{ramp} as the direction that captures trial-type independent increases or
170 decreases in preparatory activity between the onset of the stimulus and the go cue in DR trials[61,62,67,68]. This non-
171 selective ramping has been thought to represent an urgency or timing signal[69–72]. Finally, we defined $CD_{context}$, the
172 direction that best differentiates activity during the inter-trial interval of DR and WC trials (see **Methods**).
173 Projections along $CD_{context}$ revealed that context is encoded in the ALM throughout each trial (**Fig. 2d**) with strong
174 modulation at the onset of the response epoch.

175
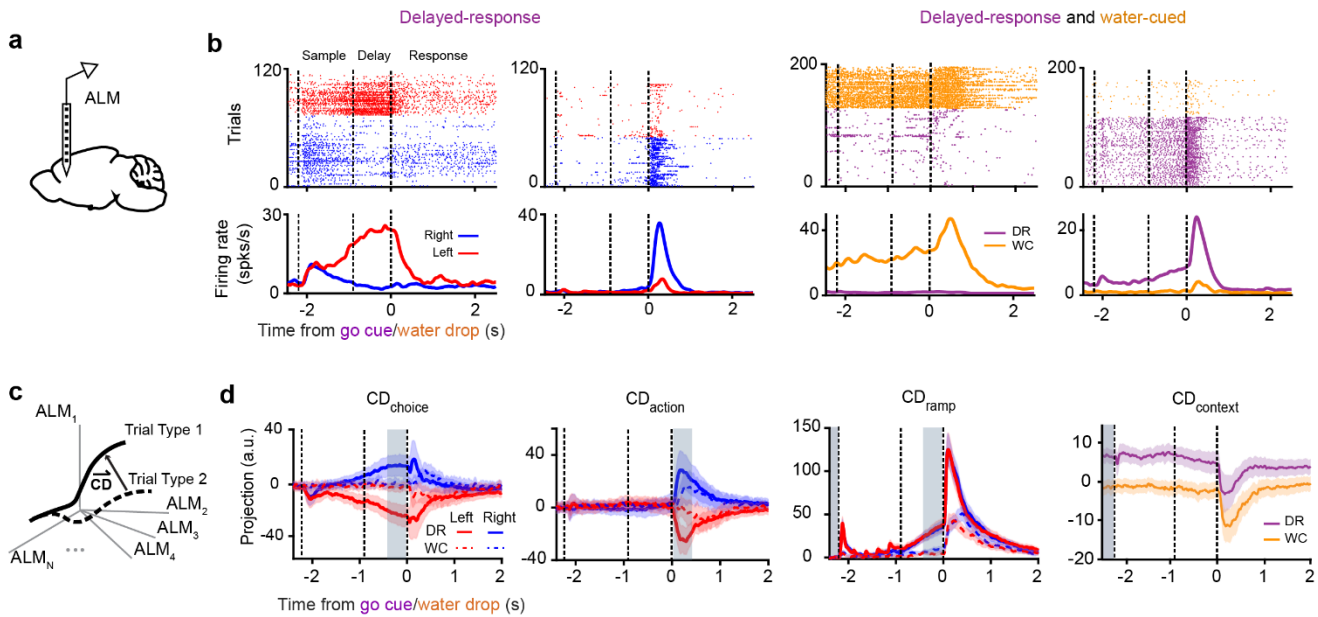
176
177 **Figure 2 – Single cell activity and population dynamics encode task-relevant cognitive and motor processes. a.** Schematic of silicon
178 probe recordings in the anterolateral motor cortex (ALM). **b.** Spike rasters (*top*) and peri-stimulus time histograms (PSTH; *bottom*) for four
179 example units in the ALM. Units show selectivity for trial type (left vs. right) and context (DR vs. WC) during all task epochs. PSTHs for
180 DR and WC tasks shown on right are averages of equal numbers of left and right trials. **c.** Schematic illustrating identification of coding
181 directions (CD). Coding directions are defined as directions in state space that maximally separate activity between trajectories defined by
182 trial types (CD_{choice}, CD_{action}), context ($CD_{context}$), or time points (CD_{ramp}). **d.** Projections along each of four defined CDs. Gray shaded
183 regions indicate time points used for CD estimation. Mean and 95% confidence intervals of bootstrapped distributions shown.

184

185 In addition to neural activity putatively related to these cognitive processes, we also examined neural signals
186 associated with the execution of movements. We defined an additional coding direction, CD_{action}, as the direction
187 that captures trial-type selective changes in neural activity that emerge after the go cue. Projections of neural activity
188 along CD_{action} robustly encoded movement direction in the ALM, as expected. Together, these four coding
189 directions explained $53 \pm 11\%$ (mean $\pm$ s.d.) of the variance in trial-averaged neural data (**EDFig. 2b**) We focus our
190 analyses on these four population-level signals, which putatively encode ALM dynamics associated with cognitive
191 and motor processes in the two-context task-switching paradigm.

Uninstructed movements related to preparatory dynamics

We next examined uninstructed movements in the DR task and their correlation with both task variables and preparatory dynamics (**Fig. 3**). We found that animals frequently performed uninstructed movements that were correlated with trial type (**Fig. 3a**) and time within each trial. On single trials, upcoming choice could be decoded from uninstructed movements beginning immediately after the presentation of the sample tone, with accuracy increasing throughout the delay epoch (**Fig. 3b**).

Not only were uninstructed movements related to the animal's upcoming actions, but they were highly correlated with preparatory dynamics on a trial-by-trial and moment-by-moment basis. The onset and magnitude of uninstructed movements often coincided with the onset and magnitude of choice selectivity and ramping (**Fig. 3c,e**). We used cross-validated multiple linear regression to predict projections along CD_{choice} and CD_{ramp} on a trial-by-trial basis from captured kinematic features of movement. Model predictions were often highly correlated with motor planning signals, indicating a close relationship between animals' uninstructed movements and preparatory dynamics (**Fig. 3d,f**; CD_{choice} : $R^2 = 0.41 \pm 0.23$, mean $\pm$ s.d across sessions, CD_{ramp} : $R^2 = 0.48 \pm 0.23$, $n = 25$ sessions), although this relationship was variable across animals and sessions (**Fig. 3d,f,i bottom row**) and variable in the kinematic features that were most predictive (**EDFig. 3a-c**). This variability is consistent with other studies[73] and highlights the need for analytical methods for assessing the relationship between neural signals and related movements on a session-by-session basis.

To further understand the relationship between uninstructed movements and preparatory dynamics, we trained additional animals on a randomized delay task in which the timing of the go cue cannot be anticipated[65]. Incorporating uncertainty into the length of the delay epoch leads to a qualitative change in population-level choice selectivity. Selectivity in CD_{choice} projections emerges earlier than in the standard fixed-delay DR task (**Fig. 3h** *top right*; fixed: 0.61 ± 0.11 s from delay onset, $n = 25$ sessions; randomized: 0.16 ± 0.19 s, $p = 2.4 \times 10^{-12}$, $n = 19$ sessions, two-sided t-test; **Fig. 3h**, *top left*), suggesting that motor plans are prepared prior to the earliest possible go cue time[65]. We found that the timing of uninstructed movements, too, shifted in an analogous fashion (**Fig. 3h**, *bottom*; fixed: 0.58 ± 0.43 s from delay onset; randomized: 0.19 ± 0.39 s, $p = 0.01$, two-sided t-test). Projections along CD_{choice} remained predictable from uninstructed movements on a single-trial level (**Fig. 3h**; average R^2 across sessions: 0.38 ± 0.20, $n = 19$ sessions), providing further evidence of the tight link between preparatory dynamics and uninstructed movements.

Uninstructed movements related to behavioral context

We next compared uninstructed movements across task blocks in the two-context paradigm (**Fig. 4**). We found that animals perform qualitatively different uninstructed movements in each behavioral context, despite both contexts requiring instructed movements to the same targets (**Fig. 4a**). Context could be decoded from kinematic features of movement across epochs – including during the ITI, in which external contextual cues were absent (**Fig. 4b**, *left*). The time-course of context decoding from neural population data and from movement kinematics was also similar (**Fig. 4b**, *right*).

We sought to understand whether trial-to-trial variability in the neural representation of context-encoding could be predicted from uninstructed movements. We again trained a multiple linear regression model to predict single-trial projections along $CD_{context}$ from kinematic features and found that, like putative choice and urgency dynamics, context-selective signals could be predicted with high fidelity (**Fig. 4c,d**; $R^2 = 0.49 \pm 0.22$, $n = 12$ sessions).

Taken together, these findings suggest that dynamics along CD_{choice}, CD_{ramp}, and $CD_{context}$ could be associated with uninstructed movements and/or the cognitive processes related to the anticipation and planning of upcoming instructed movements and encoding of task context.
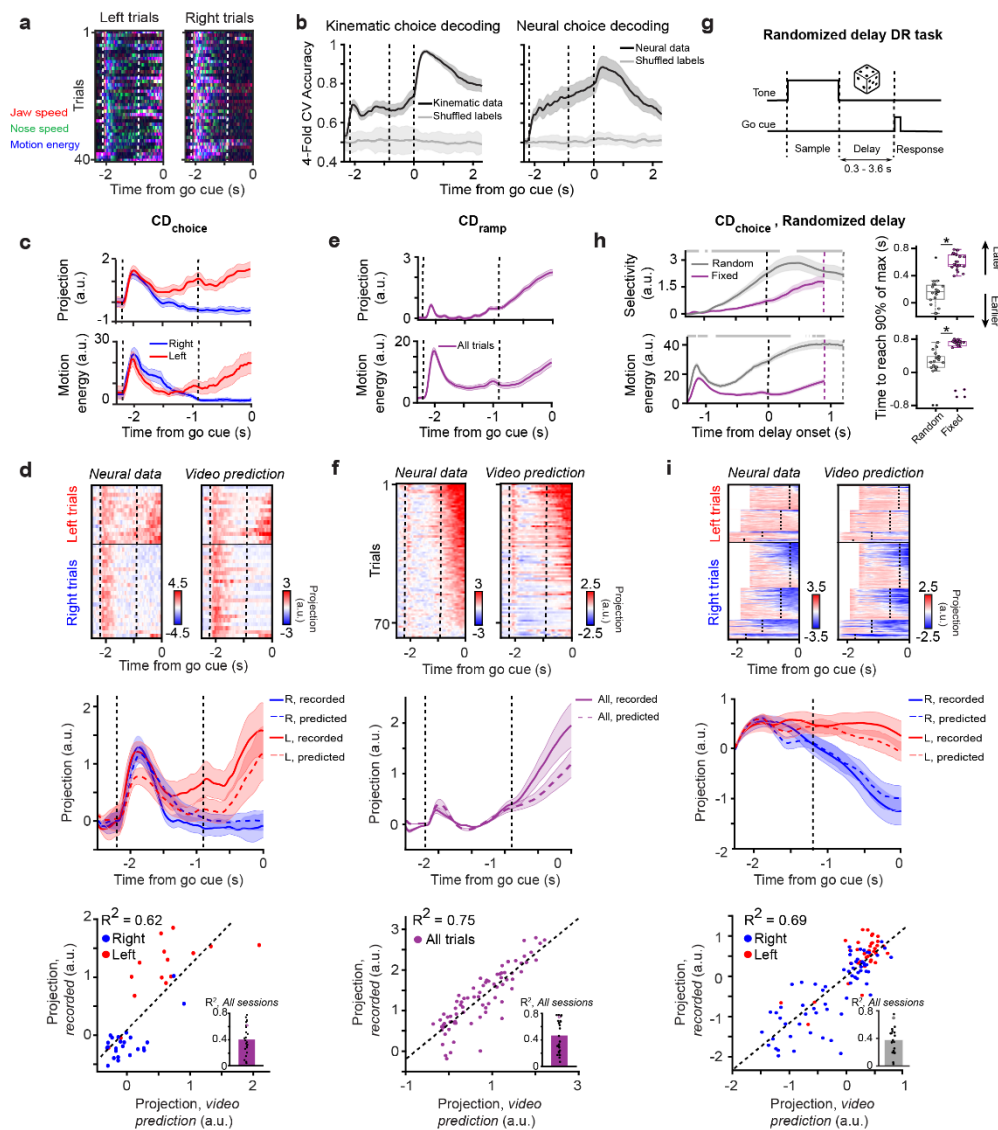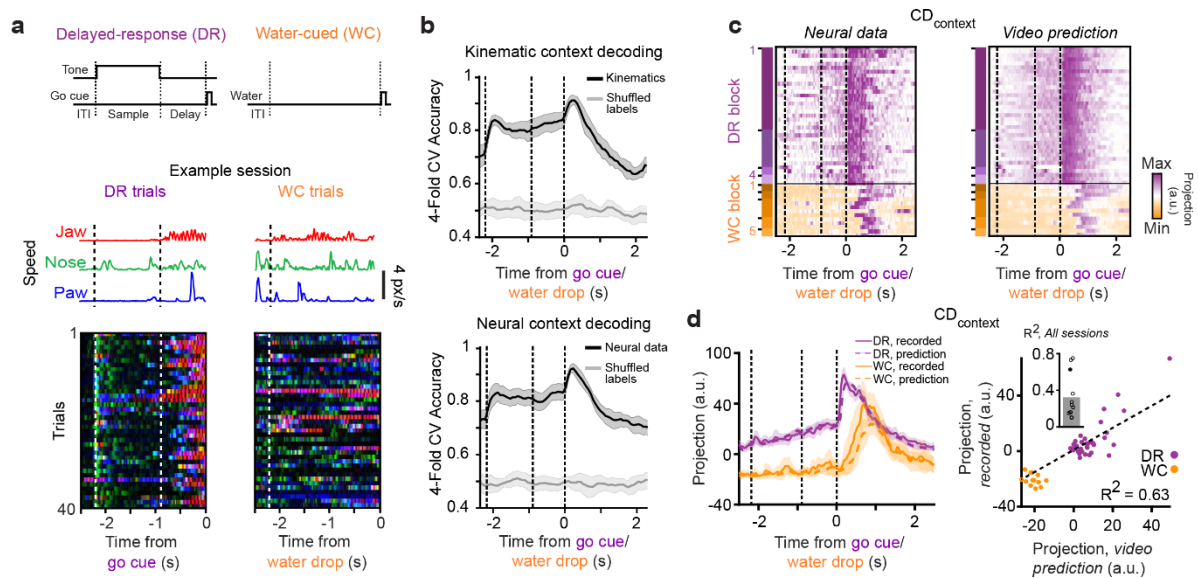
Figure 3 - Uninstructed movements are tightly linked to putative planning dynamics. a. Choice-dependent uninstructed movements. Overlayed trajectories from a random subset of DR trials in an example session. In this example, uninstructed movements are prominent on left, but not right, trials during the delay epoch. **b.** Choice (left vs. right) decoding from kinematic features and neural population data. Gray lines denote shuffled choice labels. **c.** *Top*, average projection onto CD_{choice} on left (*red*) and right (*blue*) trials for the example session depicted in (a). *Bottom*, average motion energy for all correct left and right trials. **d.** Observed and video predictions of single-trial projections of neural activity onto CD_{choice} (see **Methods**) for the same example session as in (a). *Top*, Heatmap of observed and predicted single-trial projections. Trials are sorted by the observed average projection magnitude in the late delay, with left and right trials sorted separately. *Middle*, trial-averaged CD_{choice} projections and predictions. *Bottom*, scatter plot of the average delay epoch projection of neural data onto CD_{choice} versus corresponding video predictions. Dots denote single trials and dashed line denotes linear fit. *Inset*, R^2 values for all sessions ($n = 25$ sessions). Open circle denotes the example session in (a). **e.** Same as (c) but for CD_{ramp} (different example session). Left and right hits are grouped (*purple*). **f.** Same as (d) but for CD_{ramp}. Same session as (e). **g.** Schematic of the randomized delay task. The delay epoch duration was randomly selected from six values (see **Methods**) with frequencies following an exponential distribution. **h.** Differences in choice selectivity and uninstructed movements between the randomized and fixed DR tasks. *Top left*, selectivity in CD_{choice} projections averaged across sessions for randomized delay (*gray*; $n = 19$ sessions) and fixed delay (*purple*; $n = 25$ sessions) tasks. Vertical lines indicate time of delay onset (*black*), go cue for the fixed delay (*purple*) and or go cue for the randomized delay (*gray*). Only trials with a delay duration of 1.2 s are shown for the randomized delay task for clarity. Gray bar at the top denotes timepoints where the slopes of the curves are significantly different ($p < 0.05$, two-sided *t*-test). *Bottom left*, same but for motion energy. *Top right*, time relative to delay onset that selectivity in CD_{choice} projections reaches 90% of its maximum value. Colored dots, individual sessions; black dots, outlier sessions. Asterisk denotes significant difference ($p < 0.05$, two-sided *t*-test) between latencies in randomized vs. fixed delay sessions. *Bottom right*, same but for session-averaged motion energy. **i.** Same as (d) for an example session of the randomized delay task. *Top*, trials with delay durations of 0.3, 0.6, 1.2, and 1.8 s are shown. *Middle* and *bottom*, trials with delay duration of 1.2 s only. Lines with shaded regions depict mean and 95% confidence intervals of bootstrapped distributions throughout.

Figure 4 - Uninstructed movements are closely related to the neural encoding of context. a. Schematic of tasks (*top*) and context-dependent uninstructed movements. Jaw/nose/paw movements on an example trial (*middle*) and overlayed trajectories of uninstructed movements across an example session (*bottom*) for DR task (*left*) and WC task (*right*). **b.** Context decoding from high-speed video (*top*) and neural data (*bottom*) as a function of time across all sessions. Gray lines denote shuffled context labels. **c.** *Left*, heatmap of single-trial projections of neural data onto CD$_{context}$. *Right*, CD$_{context}$ projections predicted from video in an example session. The chronological DR or WC block within the session is denoted by purple and orange rectangles, respectively, on the left of each plot. **d.** *Left*, trial-averaged projection of neural data onto CD$_{context}$ and predictions from video (*dotted lines*) for the example session illustrated in (c). *Right*, scatter plot of average projection of neural data onto CD$_{context}$ during the ITI versus average video prediction. Dots denote single trials; dashed line, line of best fit. *Inset*, R² values for all sessions ($n = 12$ sessions). Filled circle denotes the example session in (c). Lines with shaded regions depict mean and 95% confidence intervals of bootstrapped distributions throughout.

Subspace decomposition of neural activity

We next examined whether neural signals encoding task variables could be isolated from movement-related signals, despite their correlation in time. We hypothesized that if the neural dynamics associated with cognitive and motor processes are separable, their components in the ALM should be driven by distinct latent signals.

Previous theoretical work demonstrated a simple mechanism that explains how neural activity can vary dynamically while ensuring that specific variables remain stably encoded[50]. In this formalism, a variable of interest may be decoded from a neural population, perhaps by a downstream circuit, through a linear transformation matrix, W, which could be taken to follow from a particular pattern of synaptic connectivity. If the dimensionality of neural activity is larger than the dimensionality of the output signals decoded (i.e. if W is not square), then W will have a null space - dimensions along which neural activity can vary without affecting the decoded output[50].

Applying this idea to recordings from the primate motor cortex demonstrated that motor planning dynamics are confined to the null space of a linear transformation between motor cortical activity and muscle activation[39], thereby allowing motor planning signals to evolve dynamically in a manner that is independent of motor output. The orthogonal complement to this output-null subspace is the output-potent subspace; changes in activity along output-potent dimensions were then associated with changes in muscle activation[39].

Subsequent work identified analogous subspaces of neural activity in the primate motor cortex as the orthogonal subspaces that capture the most variance in neural activity during the delay and response epochs of a delayed-response task to capture preparatory and movement-related activity, respectively[40]. This approach is effective when preparatory and movement-related dynamics are confined to distinct temporal epochs and when neural activity is exclusively related to motor preparation and motor execution, respectively, in those epochs. This approach is convenient in that it avoids the need to measure muscle activation or any other descriptor of motor output. Importantly, it also avoids the need to explicitly model the transformation between neural activity and motor output as a linear transformation. This transformation is, in general, unknown and can be highly nonlinear, particularly

for movements directly controlled by central pattern generators, such as those that support much of the behavioral repertoire of rodents (e.g. locomoting, breathing, whisking, licking, chewing, vocalizing, swallowing, etc.).

We sought to determine if this computational framework could be used to isolate the neural dynamics associated with instructed and uninstructed movements from dynamics related to the encoding of choice, urgency, and context in our paradigm. Following the approach of Elsayed et al.[40] we identified subspaces that maximally capture variance in trial-averaged neural activity in the delay and response epochs of our DR trials (**Fig. 5a** and **Methods**). We found that dynamics within 'delay' and 'response' subspaces were confined to the delay and response epochs, respectively, closely resembling results observed in primates[40] (**Fig. 5b-d**). This outcome is expected when trial-averaged dynamics in different epochs occupy subspaces that are largely orthogonal[40]. However, activity within both subspaces remained highly correlated with uninstructed movements on single trials (**Fig. 5b,e,f**), suggesting that movement-related dynamics were not restricted to the 'response' subspace using this analytical framework. This follows from the assumption that planning- and movement-related processes are strictly confined to distinct task epochs, which was not the case in our paradigm. Uninstructed movements were expressed across all task epochs (**Figs. 1,3,** and **4**).

Subspace decomposition of single-trial neural activity
To avoid these limitations, we modified this analytical approach in two ways. First, because uninstructed movements vary considerably from trial-to-trial, we avoided analyses of trial-averaged data and focused on single-trial data. Second, rather than identifying subspaces capturing variance during the delay (when no movement is assumed) and response epochs, we instead annotated all time points across a session in which animals were moving and all time points at which animals were stationary. This could be straightforwardly achieved using a threshold on motion energy (calculated as the magnitude of frame-by-frame changes in images captured by video). We then found the orthogonal subspaces that best explained variance during all time points across a session at which animals were stationary and moving (**Fig. 5h**). We termed the resulting subspaces 'movement-null' and 'movement-potent' subspaces. The movement-potent subspace contains dynamical patterns typically associated with movement. Patterns that are observed in the absence of movements – those likely related to cognitive and other 'internal' processes – are contained within the movement-null subspace. Following this approach, we found that activity within the two subspaces together explained 72% of the variance in single-trial neural activity (movement-null: 30 ± 9.5%, mean ± s.d.; movement-potent: 42 ± 8.7%; n = 25 sessions). Neural dynamics in the movement-potent subspace were correlated with motion energy on single trials, as might be expected (**Fig. 5i,l,m**). Naively, movement-null subspace activity might be expected to be similarly anticorrelated with motion energy because that subspace is constructed to specifically capture variance during periods of animal stationarity. This outcome was largely not observed. Rather, movement-null subspace activity did not display a consistent relationship with movement (**Fig. 5i,l,m**) suggesting that these 'internal' dynamics were not only prominent in the absence of movement, but persisted during movement as well, in line with the supposition that cognitive processes can persist during movement.

Uninstructed movements were commonly observed during the delay epoch of DR trials, during motor planning, and were highly correlated with putative choice and urgency signals (**Fig. 3c-h**). We examined whether the movement-potent subspace might then inadvertently capture choice or urgency dynamics that are correlated in time with movements. To examine this possibility, we examined movement-null and movement-potent subspaces estimated using trials from the WC context only. Here, the movement-potent subspace is determined in a context in which choice and urgency signals are absent[23] (**Fig. 2d** and **EDFig. 4c**), precluding the possibility that dimensions of neural activity related to choice and urgency are inadvertently assigned to the movement-potent subspace due to their correlation with movement. This approach yielded subspaces that were highly similar (**EDFig. 4d-f**). In another control, examining movement-null and movement-potent subspaces estimated only using data recorded during the response epoch of both tasks, when planning and urgency dynamics should be minimal, again yielded similar results (**EDFig. 4g-i**). Finally, we estimated the movement-null subspace as the subspace defined by the top principal components of activity recorded during periods of stationarity and then determined the movement-potent subspace as the top principal components of dynamics not already captured in the movement-null subspace. This latter procedure, which is highly conservative in avoiding the spurious assignment of internal dynamics to the movement-potent subspace, again yielded similar results (**EDFig4. j-l** and **Methods**). Together, these observations suggest that the movement-potent subspace indeed captures movement-related signals, and not dynamics related to internal processes that are somewhat correlated in time with movements.

344   We hypothesized that activity in the movement-null and movement-potent subspaces should capture variance in
345   neural activity across all task epochs. Animals may think and move simultaneously; thus, it follows that internal
346   dynamics contained in the movement-null space may be present during the response epoch as well. Additionally,
347   uninstructed movements occur during both the sample and delay epochs, concurrent with stimulus and choice
348   encoding. Thus, we should also observe dynamics within the movement-potent subspace during all task epochs.
349   As expected, activity within movement-null and movement-potent subspaces captured variance across epochs (**Fig.**
350   **5k**). Interestingly, the proportion of units with activity largely confined to the movement-potent subspace was larger
351   than expected by chance (**Fig. 5n** and **EDFig. 5b**; $p = 6 \times 10^{-19}$, $n = 483$ single units, see **Methods**), and larger than
352   when subspaces were identified from trial-averaged data here (**Fig. 5g**) and in non-human primates[39]. This
353   observation suggests the identification of neuronal populations engaged solely in motor processes that could not be
354   identified without properly accounting for uninstructed movements.

355   One of the few parameters associated with this procedure is the choice of the dimensionality of the movement-null
356   and movement-potent subspaces. We examined whether varying the dimensionality of each subspaces (from four
357   to 13) influenced these results. We found our results to be largely insensitive to subspace dimensionality (**EDFig.**
358   **6a-c**), again suggesting minimal sensitivity to choice of parameters.

359   **Internal and movement-related dynamics during motor planning**
360   The movement-potent subspace may contain at least three classes of movement-related neural dynamics: (1) motor
361   commands (and efference copies), (2) sensory feedback related to movements, and (3) internal dynamics that are
362   present *exclusively during periods of* movement. That is, if a particular internal process is "embodied," in the sense
363   that it is mediated by the same latent dynamics as responsible for associated movements – and thus always observed
364   in the presence of those movements - then we would expect to find those latent dynamics wholly contained within
365   the movement-potent subspace (**Fig. 6c**). Dynamics supporting internal processes which are independent of
366   movements should be contained within the movement-null subspace (**Fig. 6a**). Between these extremes, we expect
367   to observe dynamics within both subspaces when a particular internal process (with associated latent dynamics in
368   the movement-null subspace) biases the expression of movements (with associated latent dynamics in the
369   movement-potent subspace) (**Fig. 6b**). In that latter case, internal processes may appear correlated with movements
370   despite being largely mediated by distinct latent dynamics.

371   To evaluate these possibilities, we examined whether putative cognitive signals (illustrated in **Fig. 2**) evolved within
372   the movement-potent and/or movement-null subspaces. We found choice selectivity – dynamics that differentiate
373   left and right DR trials – in both subspaces. The existence of choice dynamics in the movement-null subspace
374   indicates an internal representation of choice that is separable from dynamics related to the execution of choice-
375   related uninstructed movements (see **Fig. 6b**). The average time courses of choice dynamics in these subspaces
376   displayed subtle, yet notable, differences, as did their expression on error trials. Selectivity emerged quickly
377   following stimulus presentation in the movement-null subspace and did not change significantly through the delay
378   epoch (**Fig. 7a**; $p > 0.05$, paired t-test comparing selectivity during last 100ms of sample and delay epochs, $n = 25$
379   sessions **EDFig. 7c**) consistent with an internal representation driven by sensory input. On error trials, selectivity
380   in the movement-null subspace initially followed the same trajectory as correct trials but decayed following stimulus
381   offset. In the movement-potent subspace, in contrast, selectivity increased slowly during the sample epoch and
382   continued to increase monotonically during the delay epoch ($p = 3 \times 10^{-13}$, paired t-test comparing selectivity during
383   last 100ms of sample and delay epochs, $n = 25$ sessions; $p = 1 \times 10^{-5}$ comparing change in selectivity during the delay
384   epoch in movement-potent and movement-null subspaces; **EDFig. 7b**), and no significant movement-potent
385   subspace selectivity emerged on error trials. These observations suggest that sensory stimuli initially drive
386   appropriate dynamics within the movement-null subspace on error trials, but that choice is not encoded stably and
387   does not engage movement-potent dynamics related to uninstructed movements.

388   Although the trajectories of choice dynamics in each subspace shared some similarities in trial-averaged data (**Fig.**
389   **7a**), the existence of choice dynamics in both subspaces implies that they must differ markedly on single trials.
390   The onset and magnitude of activity along the component of CD_{choice} within the movement-potent subspace
391   tracked trial-type selective motion energy on a moment-by-moment basis (**Fig. 7b, c**), as expected, while there
392   was no consistent relationship between motion energy and activity along the component of CD_{choice} in the
393   movement-null subspace. Following the go cue, transient responses accompanying movement initiation were
394   absent from the movement-null subspace (**EDFig. 7a**), further suggesting the existence of choice dynamics which
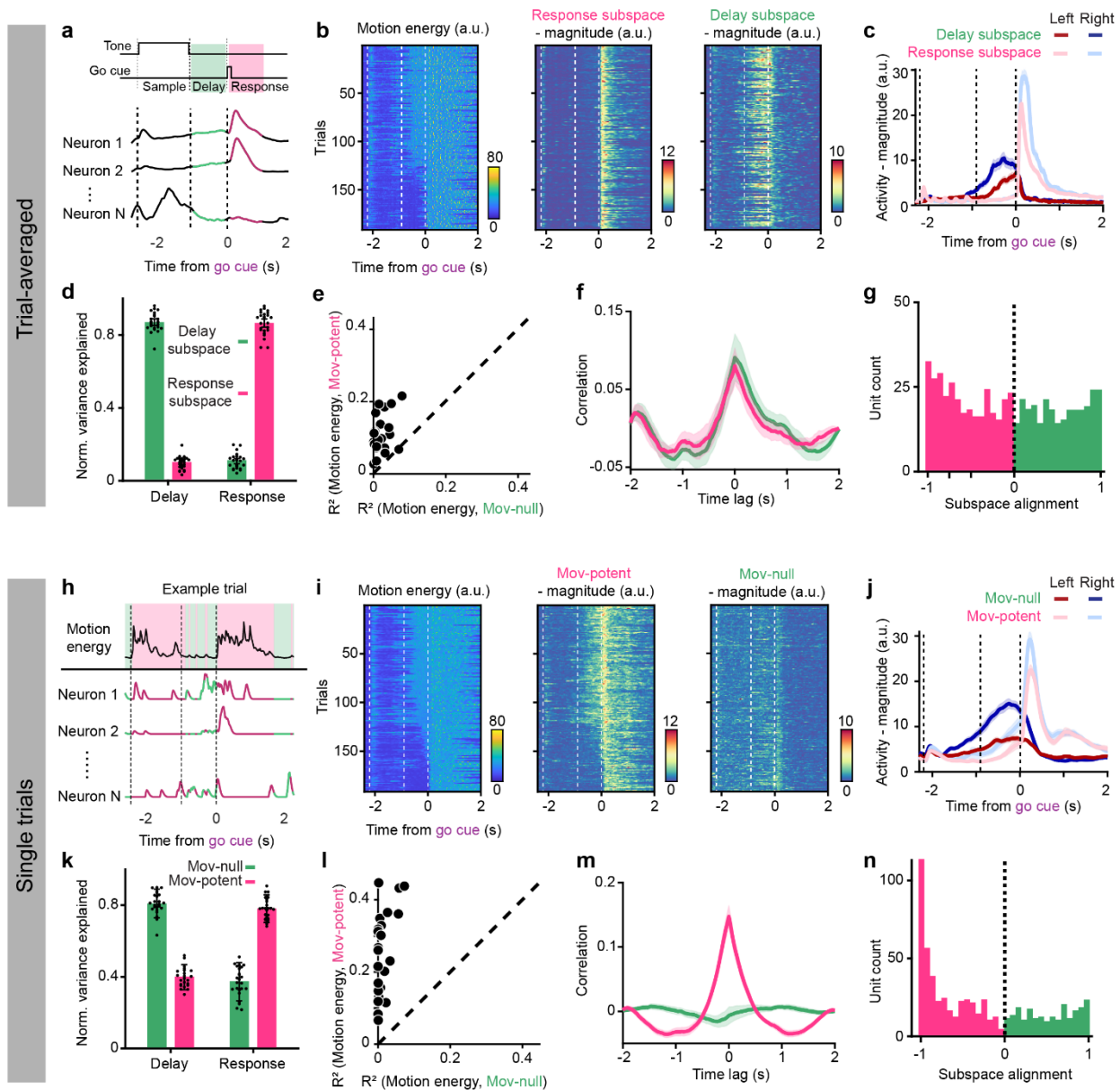
**Figure 5 – Subspace decomposition of neural activity using trial-averaged and single-trial data. a.** Schematic of the approach for estimating delay (*green*) and response (*pink*) subspaces from trial-averaged neural data. Delay and response subspaces are determined as the orthogonal subspaces that maximally contain the variance of neural activity in the delay and response epochs, respectively. Correct trials from the DR context were used to identify subspaces. **b.** Activity during DR trials within each subspace for an example session. *Left*, motion energy across trials. *Middle*, sum-squared magnitude of activity in the response subspace. *Right*, sum-squared magnitude of activity in the delay subspace. Trials sorted by average delay epoch motion energy. **c.** Sum-squared magnitude of activity in delay and response subspaces during DR lick-left and lick-right trials for an example session. Mean and standard error across trials shown. **d.** Normalized variance explained of the neural data during DR trials by the activity in the delay and response subspaces during the delay and response epochs. Delay and response subspaces selectively capture activity in the delay and response epochs, as expected. Points indicate sessions, bar height indicates the mean across sessions, and error bars indicate standard deviation across session ($n = 25$ sessions). **e.** Variance explained (R^2) of motion energy by the sum-squared magnitude of activity in the delay and response subspaces using single-trial DR and WC data. Each point represents the mean across trials for a session ($n = 25$ sessions). **f.** Cross-correlation between motion energy and activity in the delay and response subspaces using single-trial DR and WC data. Lines indicate mean across sessions and shaded region represents standard error of the mean across sessions ($n = 25$ sessions). **g.** Subspace alignment for single units across all sessions ($n = 483$ single units, see **Methods**). Values closer to 1 indicate that more variance of a unit's activity is contained within the preparatory subspace. **h.** Schematic of the approach for estimating movement-null and movement-potent subspaces from single-trial data. Motion energy is used to annotate when an animal is moving (*pink*) or stationary (*green*). These labels are then applied to single-trial neural data. Movement-null and movement-potent subspaces are determined as the orthogonal subspaces that maximally capture the variance of neural activity during periods of quiescence and movement, respectively. Trials from both DR and WC contexts were used to identify subspaces. **i-n.** Same as (b-f) but using the single-trial approach for estimating movement-null and movement-potent subspaces.
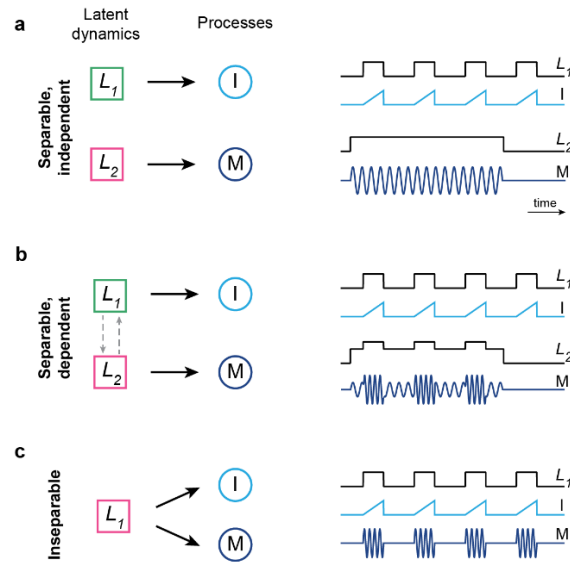
Figure 6 – Schematic of potential relationships between internal and movement-related dynamics. a. Internal and movement-related dynamics that are independent and separable. *Left,* schematic depicting an internal process (I) and a motor process (M) that are each governed by separate latent dynamics, L_1 and L_2, respectively. L_1 and L_2 evolve within the movement-null (green) and movement-potent (pink) subspaces, respectively. *Right,* cartoon time series of separable, independent latent dynamics (L_1 and L_2) and related processes (I and M). **b.** Same as (a) in the case of latent dynamics which are separable but dependent. I and M may be loosely correlated in time. **c.** Same as (a) and (b) in the case of inseparable processes governed by a single set of latent dynamics (L_1).

are separable from ongoing movement dynamics. Importantly, we found that many single units contribute to either the movement-null or movement-potent subspace representations of CD_{choice}, but not both (**Fig. 7d** and **EDFig. 6d**), providing additional evidence of dynamics that are not only separable, but encoded by distinct populations of neurons (**Fig. 7d**) within the ALM microcircuit.

In contrast, we found that ramping dynamics were mostly confined to the movement-potent subspace (**Fig. 7e**) – perhaps surprising given that ramping activity has been interpreted as an internal urgency or timing signal[69–72]. This observation remained consistent when estimating movement-null and movement-potent subspaces using only WC trials or using only the response epoch of WC and DR trials (**EDFig. 8a**), when ramping dynamics were absent, confirming that ramping dynamics were not observed in the movement-potent space because of the mis-assignment of internal ramping dimensions to the movement-potent subspace because of their correlation in time with movement. We further searched for the existence of movement-null subspace ramping dynamics by explicitly identifying the dimension within the movement-null and movement-potent subspaces that maximized ramping dynamics – which could be different than the dimension that maximized ramping within the full activity space – and again failed to identify a prominent ramping signal in the movement-null subspace (**EDFig. 8b**). The relative paucity of ramping dynamics in the movement-null subspace suggests that they are not readily separable from associated movements in the ALM in our behavioral paradigm (see **Discussion**).
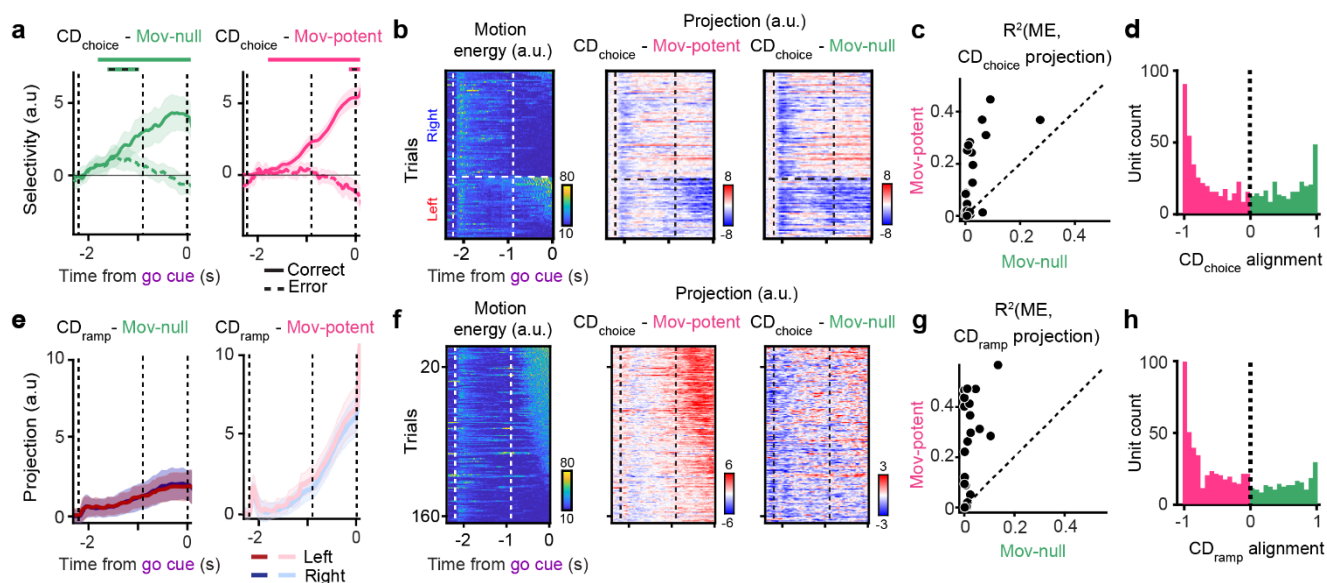
Figure 7 – Subspace decomposition allows for the re-examination of population measures of motor planning. a. Selectivity (neural projections on lick-right trials minus lick-left trials) of movement-null (*left*) and movement-potent (*right*) subspace activity when projected along CD_{choice}. Mean and 5-95% CI of the bootstrap distribution for correct (solid) and error (dashed) trials shown. Horizontal bars (solid lines - correct trials; solid lines with black dashes - incorrect trials) above plot indicate when the selectivity trace is significantly different from zero ($p < 0.05$, one-sided test, bootstrap). **b.** Projections along CD_{choice} in the movement-potent subspace (*middle*), but not the movement-null subspace (*right*), follow the time-course and magnitude of motion energy (*left*) on single lick-left and lick-right trials (example session). **c.** Variance explained (R^2) of motion energy by projections along CD_{choice} in the movement-null or movement-potent subspace on single trials. Each point is the average across all trials in a session. **d.** Distribution of single unit alignment with CD_{choice} ($n = 483$ single units, see **Methods**). Distribution of movement-potent tuned units (alignment ≤ -0.8) was significantly different than expected by chance ($p = 1x10^{-13}$, see **Methods**). Similarly, distribution of movement-null tuned units (alignment ≥ 0.8) was significantly different than expected by chance ($p = 7x10^{-12}$). **e.** Projection of movement-null (*left*) and movement-potent (*right*) subspace activity along CD_{ramp} on lick-left and lick-right trials. Mean and 95% CI of the bootstrap distribution for correct trials shown. **f-h.** Same as (b-d) for CD_{ramp}. **h.** Distribution of single unit alignment with CD_{ramp} ($n = 483$ single units). Distribution of movement-potent tuned units (alignment ≤ -0.8) was significantly different than expected by chance ($p = 6x10^{-14}$). Similarly, distribution of movement-null tuned units (alignment ≥ 0.8) was significantly different than expected by chance ($p = 1x10^{-12}$).

A persistent movement-null subspace representation of context

Next, we examined projections of activity along $CD_{context}$ in each subspace (**Fig. 8a**). We found robust contextual selectivity in both subspaces, consistent with the interpretation that the ALM contains both an internal representation of context and activity related to context-dependent movements. The transient, response-epoch dynamics observed along $CD_{context}$ (**Fig 2d,** *far right*) were entirely contained within the movement-potent subspace (**Fig. 8a**) likely indicative of subtle context-specific differences in instructed movements. We then compared context selectivity (the difference in projections onto $CD_{context}$ on DR vs. WC trials) on trials with high motion energy during the ITI ('High move' trials) and trials with little or no ITI motion energy ('Low move' trials). Context selectivity within the movement-null subspace was indistinguishable in 'High move' and 'Low move' trials. In contrast, context selectivity within the movement-potent subspace was reduced by 72% on 'Low move' trials (**Figs. 8b,c**; Full population: selectivity reduced by 0.101 ± 0.092, mean ± s.d., $p = 0.003$; movement-null: 0.026 ± 0.050, $p = 0.095$; movement-potent: 0.098 ± 0.082, $p = 1.6x10^{-3}$, paired t-test; Δ selectivity between 'High move' and 'Low move' trials in movement-null vs. movement-potent: $p = 9.5x10^{-3}$, paired t-test). The magnitude and timing of the reduction in movement-potent subspace context selectivity mirrored the reduction in motion energy on 'Low move' trials (**Fig. 8b**, *bottom*). Together, these observations demonstrate that the movement-null – but not movement-potent – subspace contains a stable representation of context that is unchanged in the presence of both instructed and uninstructed movements. Further, we found that largely distinct populations of single neurons contribute preferentially to the movement-null and movement-potent representations of context (**Fig. 8d**). These observations suggest that the analysis of context-dependent dynamics without subspace decomposition indeed spuriously conflated separate latent dynamics, encoded by different populations of neurons, likely responsible for internal

476 representations of context (contained within the movement-null subspace) and related context-dependent
477 movements (contained in the movement-potent subspace).

478 **Encoding of tongue kinematics in the movement-potent subspace**
479 Finally, we asked whether trial-type dependent activity following the go cue relates to movement, according to
480 previous suppositions[58,6458,64] (**EDFig. 10**). Left-right selectivity along CD_{action} existed within both the movement-
481 null and movement-potent subspaces (**EDFig. 10a**), although the magnitude of selectivity in the movement-null
482 subspace was substantially smaller in magnitude. Interestingly, on error trials, activity along CD_{action} flipped to
483 resemble that of the other trial type in the movement-null subspace but flipped asymmetrically within the
484 movement-potent subspace. This asymmetry closely corresponded to an asymmetry in tongue angle, with incorrect
485 movements directed to less extreme angles when directed to the left, on average (**EDFig. 10b,c**). The component
486 of CD_{action} within the movement-potent subspace also better tracked moment-to-moment changes in tongue angle
487 during the response epoch (**EDFig. 10d,e**; $p = 2 \times 10^{-8}$, paired t-test between movement-null and movement-potent
488 variance explained of tongue angle, $n = 25$ sessions). The similarity between tongue angle, a kinematic feature, and
489 dynamics only within the movement-potent representation of CD_{action} is notable, as our analytical approach to the
490 identification of subspaces does not incorporate any kinematic information. The interpretation of action dynamics
491 within the movement-null subspace remains unclear but could relate to an internal representation of the motor plan,
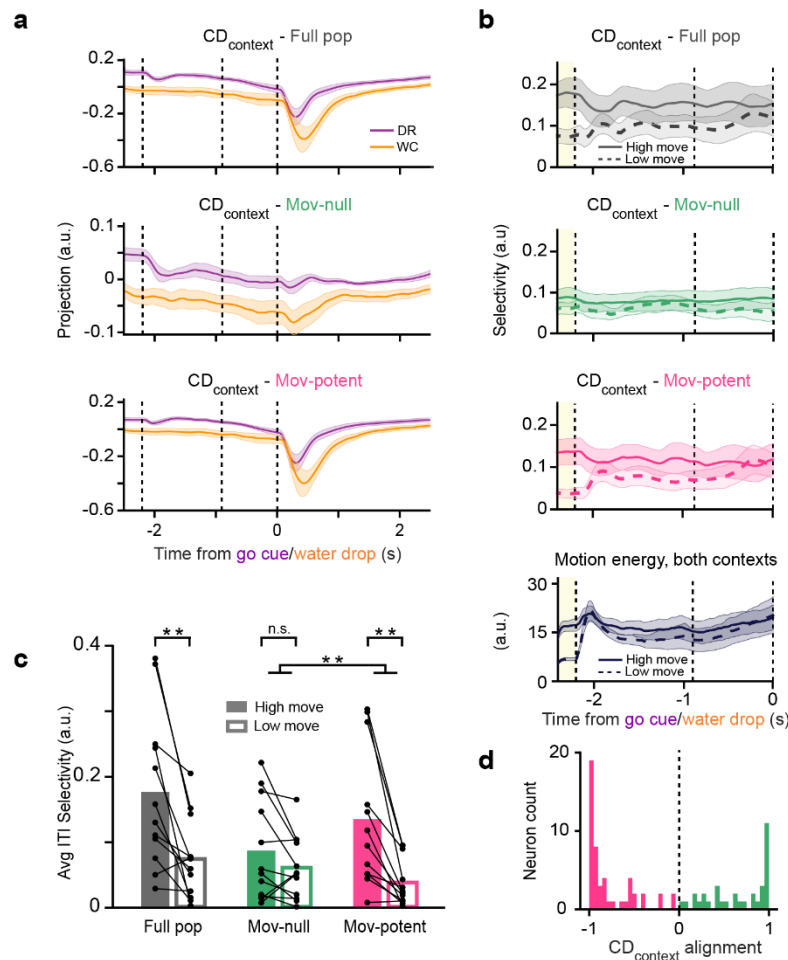492 or intention of the animal, to respond to one reward port or the other.

493
494
495
496
497
498

499

500 **Figure 8 – A persistent, cognitive representation of context in the movement-null subspace. a.** Projections along $CD_{context}$ on DR hit
501 trials (*purple*) and WC hit trials (*orange*) within the full population (*top*), movement-null subspace (*middle*), or the movement-potent subspace
502 (*bottom*). Solid lines denote the mean projection across sessions ($n = 12$ sessions). Note that transient response epoch dynamics are absent
503 in the movement-null subspace. **b.** *Top three panels*, selectivity in $CD_{context}$ projections (DR – WC trials) on 'high move' (*solid lines*) or
504 'low move' (*dashed*) trials. Lines denote the mean selectivity across sessions ($n = 12$) in the full space of neural activity (*top*), activity within
505 the movement-null subspace (*second*), and movement-potent subspace (*third*); *Bottom panel*, average motion energy across sessions on 'High
506 move' or 'Low move' trials. DR and WC trials are grouped together for each session. Shaded area, 95% CI across sessions. Yellow region
507 denotes ITI used to define 'High move' and 'Low move' trials. **c.** Average $CD_{context}$ selectivity during the ITI (yellow shaded region in (b))
508 for 'High move' (*filled bars*) vs. 'Low move' (*open bars*) trials. Dots denote single sessions; bars, mean across sessions ($n = 12$ sessions).
509 Asterisks denote significant differences (**, $p < 0.01$) in $CD_{context}$ selectivity (p-values from left to right comparing 'High move' vs. 'Low
510 move' trials, Full population: $p = 0.003$, movement-null: $p = 0.095$, movement-potent: $p = 1.6 \times 10^{-3}$; Δselectivity between 'High move' and
511 'Low move' trials in movement-null vs. movement-potent: $p = 9.5 \times 10^{-3}$, paired t-test). **d.** Distribution of single unit alignment with $CD_{context}$
512 (see **Methods**). Distribution of movement-potent tuned units (alignment ≤ -0.8) was significantly different than expected by chance ($p =$
513 2×10^{-8}, see **Methods**). Similarly, distribution of movement-null tuned units (alignment ≥ 0.8) was significantly different than expected by
514 chance ($p = 9 \times 10^{-6}$, $n = 84$ single units). Lines with shaded regions depict mean and 95% confidence intervals across sessions throughout.

Discussion

We aimed to understand whether the neural correlates of three cognitive variables commonly examined in sensorimotor decision-making tasks – choice, urgency, and context – were separable from the neural encoding of related uninstructed movements in the mouse ALM. We addressed this question by adapting an analytical formalism in which neural activity is decomposed into orthogonal subspaces – here, a movement-potent subspace containing dynamics related to the execution of movements and a complementary movement-null subspace containing dynamics related to cognitive and other internal processes[39,40,50]. Extending upon this framework allowed us to consider single-trial neural data recorded in the presence of uninstructed movements that can vary dramatically across trials in their timing and identity (**Fig. 5**).

Separability of choice, urgency, and context encoding from movement-dynamics

Using this approach, we demonstrated that the ALM contains neural dynamics related to encoding of choice and context that could be readily separated from movements, despite both cognitive variables being strongly correlated with movements in time (**Fig. 7** and **Fig. 8**). Choice-selective signals were present in both movement-null and movement-potent subspaces (**Fig. 7a**), consistent with the interpretation that a cognitive representation of choice within the movement-null subspace biases the probability and identity of uninstructed movements in a choice-selective manner. Supporting this interpretation, movement-null and movement-potent subspace dynamics followed similar trajectories, on average, but differed on single trials (**Fig. 7b**). Further, movement-null subspace encoding of choice exhibited features absent from encoding within the movement-potent subspace. Choice encoding increased in the presence of external stimuli, while movement-potent subspace encoding continued to increase monotonically after sensory stimuli were removed, mirroring the temporal evolution of animal's uninstructed movements. On error trials, stimulus-driven choice encoding initially evolved correctly – but only within the movement-null subspace – before decaying prior to the go cue (**Fig. 7a**). Together, these results suggest choice-related cognitive and motor processes that are governed by separable latent dynamics (**Fig. 6b**).

Context was stably encoded within the movement-null subspace during all trial epochs and the inter-trial interval (**Fig. 8a-c**). Although context was strongly represented in the movement-potent subspace as well, these dynamics were significantly reduced in the absence of movement and were also modulated by animals' instructed movements. These results suggest a persistent internal representation of context in the movement-null subspace in addition to distinct movement-potent-subspace dynamics related to context-dependent movements, again indicative of related, but separable, latent dynamics (**Fig. 6b**).

Surprisingly, ramping dynamics proposed to underlie urgency (or timing)[69–72] were principally represented in the movement-potent subspace (**Fig. 7e**) indicating the possible absence of an internal representation of urgency that can be dissociated from movements in the ALM. Although it remains possible that a separable representation of urgency exists elsewhere in the brain, our results could alternatively imply that urgency is typically embodied, or inseparable from movement, in our behavioral paradigm[74,75].

In contrast to these cognitive variables, encoding of kinematic features of movements, which were not used to determine subspaces, were confined to the movement-potent subspace (**EDFig. 10**), consistent with our interpretation of these subspaces.

Subspace decomposition

The approach to subspace decomposition presented here represents a means for assessing the issue of separability, and for isolating separable dynamics into movement-related and internal components for further analyses across a wide range of experimental preparations. This method only requires annotation of when animals are moving and utilizes a robust analytical approach that does not require fine-tuning of parameters.

A number of alternative methods have been proposed to evaluate neural dynamics associated with cognitive processes in the presence of movement. The most common approach, which assumes separability of cognitive and motor dynamics, is to parameterize movements as fully as possible and 'regress them out.' However, parameterization of movement, particularly the orofacial and postural movements that have been associated with strong, brain-wide neural dynamics[30,31,76], can be challenging. Further, this approach typically assumes a linear relationship between neural activity and kinematic (or electromyographic) variables – an assumption unlikely to hold for common movements mediated by central pattern generators and other highly nonlinear mechanisms[77–79]. Subspace decomposition is straightforward to implement under a range of experimental conditions and is entirely consistent with complex, nonlinear relationships between neural activity and movement variables, as expected for

many orofacial movements[77] and locomotion. Methods for properly interpreting cognitive signals in the presence of related movements on single trials will be vital for increasingly common experimental paradigms examining freely moving animals performing complex, naturalistic behaviors[80–90].

Determination of movement-null and movement-potent subspaces as the orthogonal subspaces containing the most variance in neural activity during periods of stationarity and movement is conservative in the assignment of dynamics to the movement-null subspace. It is more likely that dynamics associated with cognitive and other internal processes are misassigned to the movement-potent subspace than vice-versa. For example, dynamics associated with "embodied" cognitive processes that always occur during periods of movement will only be represented in the movement-potent subspace (**Fig. 6c**). Thus, the dynamics within the movement-null subspace are highly likely to indicate signals related to internal processes. Straightforward variations of this approach can be used to determine subspaces in a manner that is more conservative in assigning dynamics to the movement-potent subspace – for example, estimating subspaces from response epoch data ('instructed' movements), from WC trials (where uninstructed movements occur in the absence of choice and urgency signals) or simply through principal component decomposition of activity recorded during periods of stationarity (**EDFig. 4j-l**). Nevertheless, the similarity of results obtained using these analytical variations argue against the possibility that cognitive dynamics associated with choice and urgency were inadvertently assigned to the movement-potent subspace, due to their correlation in time with uninstructed movements, in this study.

That many individual units contribute solely to one subspace (**Figs. 5n, 7d,h, 8d**) suggests that the complementary subspaces we identify could map to distinct cell types within the underlying cortical circuit[63,91]. The suggestion that individual neurons only appear to code for either internal or movement-related variables when uninstructed movements are accounted for (**Figs. 5n, 7d,h, 8d**) underscores the importance of properly considering movements in future work focused on the roles of functionally, anatomically, and/or transcriptomically-defined cell-types in neural computation.

Our approach to subspace decomposition makes several simplifying assumptions. First, movements of the posterior torso, hindlimbs, or tail of the animal were not routinely captured via videography. It remains possible, albeit unlikely, that animals routinely perform movements confined to these portions of the body without concomitant movement of the forepaws, head, neck, face, or whiskers[26]. Periods of stationarity were no doubt algorithmically classified imperfectly and could have contained subtle movements below our threshold for detection. Second, we did not consider potential time lags between motion energy captured via videography and the dynamics associated with motor and/or sensory signals[73]. However, these time lags, on the order of a few tens of milliseconds, should be much shorter than the timescale of dynamics explored in this study. Third, the set of signals related to movement and/or cognitive processes may also be better described as occupying nonlinear manifolds rather than linear subspaces[92,93]. Subspaces (or manifolds) could also shift dynamically during behavior following changes in the activation of upstream or downstream brain regions[94,95] as a result of changes in context[16,48,96]. Considering this additional complexity may improve estimates of the dynamics associated with specific neural processes.

Variable relationships between cognition and movement

The dynamics associated with some cognitive processes and movements may be largely independent (**Fig. 6a**) – perhaps in the case of the locomotor patterns of an individual walking down the street while thinking about what they will cook for dinner. On the other hand, some cognitive processes may be embodied, in the sense that they are tightly linked to externally observable changes in the body (**Fig. 6c**), such as the relationship between arousal and changes in pupil diameter[97–99]. Between these extremes may be movements which are correlated with - but mediated by neural dynamics that are separable from - those supporting cognitive and other internal processes. The probability and identity of uninstructed movements in this study appeared related to choice and context (**Fig. 6b**), but with a high degree of trial-to-trial and moment-to-moment variability unlikely to reflect commensurate variability in the cognitive processes to which they relate. Correlations between cognitive processes and movements may also differ considerably in trained, head-fixed animals compared to naturalistic settings[83,88]. This high degree of variability in these relationships underscores the importance of developing and utilizing tools for assessing whether the neural activity supporting cognitive processes can be dissociated from those related to movements in particular experimental paradigms of interest.

The tight link between cognition and movement might suggest that some cognition-associated movements may be beneficial for behavior. For example, postural adjustments may be highly related to decisions or motor plans,

617 enabling faster reaction times and/or more accurate movements[76,100]. Movements are also essential for some internal
618 processes – those supporting active sensation of the environment surely facilitate the construction and continual
619 updating of internal models of the environment[30,46]. However, just as separability may not be consistent across
620 movements and cognitive processes, not all cognition-associated movements may have a functional role[30,101]. A
621 poker player's 'tell' may be highly related to their cognitive state, yet may not directly aid the player in the game.
622 Regardless of their functional relationship, understanding the separability of cognitive processes and associated
623 movements in a wide variety of experimental settings is essential for the interpretation of neural dynamics observed
624 during behavior.

625 **Methods**

626 *Animals*
627 This study used data collected from 17 mice; both male and female animals older than 8 weeks were used. Six
628 animals were used for the two-context task and were either C57BL/6J (JAX 000664) or VGAT-ChR2-EYFP (-/-).
629 An additional three animals, either C57BL/6J or VGAT-ChR2-EYFP (-/-) were trained only on the delayed response
630 task. A separate cohort of four animals were used in the randomized delay task (VGAT-ChR2-EYFP (+/-) or
631 VGAT-ChR2-EYFP (-/-)). Finally, four VGAT-ChR2-EYFP (+/-) animals were used in optogenetics experiments.
632 Mice were housed in a 12-hour reverse dark/light cycle room with ad libitum access to food. Access to water was
633 restricted during behavioral and electrophysiology experiments (see **Mouse behavior**). Sample sizes were not
634 determined using any statistical tests.
635
636 *Surgical procedures*
637 All surgical procedures were performed in accordance with protocols approved by the Boston University
638 Institutional Animal Care and Use Committee. For post-operative analgesia, mice were given ketoprofen (0.1 mL
639 of 1 mg/mL solution) and buprenorphine (0.06 mL of 0.03 mg/mL solution) prior to the start of all surgical
640 procedures. Mice were anesthetized with 1-2% isoflurane and placed on a heating pad in a stereotaxic apparatus.
641 Artificial tears (Akorn Sodium Chloride 5% Opthalmic Ointment) were applied to their eyes and a local anesthetic
642 was injected under the skin (Bupivacaine; 0.1 mL of 5 mg/mL solution) above the skull. The skin overlying the
643 skull was removed to expose the ALM (AP: +2.5 mm, ML: +1.5 mm), bregma, and lambda. The periosteum was
644 removed and the skin was secured to the skull with cyanoacrylate (Krazy Glue) around the margins. For
645 electrophysiology experiments, a headbar was implanted just posterior to bregma and secured with superglue and
646 dental cement (Jet™). Wells to hold cortex buffer (NaCl 125mM, KCl 5mM, Glucose 10mM, HEPES 10mM,
647 CaCl2 2mM, MgSO4 2mM, pH 7.4) during electrophysiology recordings were sculpted using dental cement and a
648 thin layer of superglue was applied over any exposed bone.
649
650 For optogenetics experiments, after headbar implantation, bone overlying frontal cortex was thinned bilaterally with
651 a dental drill and removed, exposing the frontal cortex. A glass window was then implanted over each hemisphere
652 and secured to the skull with cyanoacrylate[102]. Before performing photoinactivation experiments, any bone regrowth
653 was removed.
654
655 *Mouse behavior*
656 Following surgery, mice were allowed to recover for ~1 week and then water restricted, receiving 1.0 mL of water
657 per day. Behavioral training commenced after animals had been water restricted for 3-4 days. If animals received
658 less than 1.0 mL during training, they were supplemented with additional water.

659 All mice used in experiments were first trained on the delayed-response task with a fixed delay epoch until they
660 reached at least 70% accuracy. At the beginning of each trial, one of two auditory tones lasting 1.3 s were played;
661 the tone indicating a 'right' trial was white noise while the tone indicating a 'left' trial was a pure tone (8 kHz
662 pulses). The delay epoch (0.9 s for 12 mice, 0.7 s for 1 mouse and linearly time warped to 0.9 s) started after the
663 completion of the sample tone. Following the delay epoch, an auditory go cue was played (swept-frequency cosine
664 [chirp], 10 ms) after which animals were rewarded with ~3 μL of water for contacting the correct lickport. Lickport
665 contacts before the response epoch resulted in the current task epoch restarting, ensuring that they could not progress
666 to the next task epoch until they had stopped licking for the specified length of the current epoch. If the animal did
667 not respond within 3 s of the go cue, this was considered an 'ignore' trial, although responses were typically
668 registered within 300 ms of the go cue.

669　Mice used for the two-context task (**Figs. 1,2,4,8** and **EDFig. 1-3**) were introduced to the water-cued context after
670　they were fully trained on the delayed-response context and at least two days before the first electrophysiology
671　recording session. A behavioral session began with ~100 DR trials and was then followed with alternating blocks
672　of WC and DR trials. Each interleaved block was 10-25 trials, with no fixed block duration. All sessions started
673　with DR trials. Pilot sessions beginning with WC trials had to be terminated early due to a high 'no response' rate,
674　likely due to the mouse becoming sated early in the session. In a WC trial, all auditory cues were omitted and a ~3
675　µL water reward was presented randomly from either lickport. Trials in which the animal contacted the lickport
676　prior to the reward ('early lick') were omitted from analyses. Inter-trial intervals were randomly drawn from an
677　exponential distribution with mean 1.5 s. There were no explicit cues during the ITI to indicate to the animal which
678　context block it was in.

679　For the randomized delay task (**Fig. 3g-h**), mice were first fully trained on the fixed delay DR task (delay duration
680　of 0.9 s). The delay epoch length was then randomized – the duration was randomly selected from six possible
681　values (0.3, 0.6, 1.2, 1.8, 2.4, and 3.6 s). The probability of each delay duration being selected was assigned such
682　that it resembled a probability density function of an exponential distribution with $\tau = 0.9$ s, as in ref [65]. Animals
683　were trained on this version of the task until they became experts (> 70% accuracy and < 20% early lick rate).

685　*Videography analysis*
686　High-speed video was captured (400 Hz frame rate) from two cameras (FLIR, Blackfly® monochrome camera,
687　Model number: BFS-U3-16S2M-CS). One provided a side view of the mouse and the other provided a bottom view.
688　We tracked the movements of specific body features using DeepLabCut[52] (**Figs. 1,3,4**). The tongue, jaw, and nose
689　were tracked using both cameras while the paws were only tracked using the bottom view. Position and velocity of
690　each tracked feature was calculated from each camera. The x and y position of each kinematic feature was extracted
691　from the output of DeepLabCut. Missing values were filled in with the nearest available value for all features except
692　for the tongue. The velocity of each feature was then calculated as the first-order derivative of the position vector.
693　Tongue angle and length were found using the bottom camera. Tongue angle was defined as the angle between the
694　vector pointing from the jaw to the tip of the tongue and the vector defining the direction the mouse was facing.
695　Tongue length was calculated as the Euclidean distance from the jaw to the tip of the tongue.

696　Plots of kinematic feature overlays (**Figs. 1e, 3a, 4a** and **EDFig. 3**) were generated by plotting an [r, g, b] value for
697　each timepoint, *t*, where the values were specified by [KinFeature1$_t$, KinFeature2$_t$, KinFeature3$_t$]. All kinematic
698　features (speed or motion energy) were first standardized by taking the 99th percentile across time and trials and
699　normalizing to this value.

701　*Motion energy*
702　The motion energy for a given frame and pixel was defined as the absolute value of the difference between the
703　median value of the pixel across the next 5 frames (12.5 ms) and the median value of the pixel across the previous
704　5 frames (12.5 ms). Motion energy for each frame was then converted to a single value by taking the 99th percentile
705　(~700 pixels) of motion energy values across the frame. Motion energy calculated in this manner was high during
706　overt movements over small regions of pixel space, such as during whisking, while remaining relatively low during
707　passive respiration that corresponded to subtle motion across the animal's body. A threshold above which an animal
708　was classed as moving, was defined on a per session basis manually. Motion energy distributions, per session, were
709　bimodal, showing a large peak with little variance at low motion energy values and a second, smaller peak, with
710　high variance at large values. The threshold was set as the motion energy value separating these two modes. We
711　found that this method of setting the threshold captured both short and long duration movements. Alternative
712　methods, such as defining a baseline period of no movement against which to compare, were less successful due to
713　the variability in timing of the movements across trials.

715　*Photoinactivation experiments*
716　Optogenetic photoinactivation was deployed on ~30% of trials selected at random. A 'masking flash' (470 mm
717　LED's LUXEON REBEL LED) controlled by an Arduino Teensy microcontroller (100 ms pulses, at 10 Hz) was
718　delivered constantly for the duration of the session to prevent mice from differentiating control and
719　photoinactivation trials. A 488-nm laser (Coherent OBIS 488 nm LX 150 mW Laser System) was used for all
720　photoinactivation experiments. ChR2-assisted photoinactivation (**Fig. 1b,c,g-** and **EDFig. 1b-d**) was performed
721　through a cranial window[102] (see ***Surgical Procedures***), which replaced bone over the frontal cortex. Light was

722 delivered either at the start of the delay epoch, or at the start of the response epoch (only one epoch tested per
723 session). A power density of 1.5 mW/mm^2 was used for all photoinactivation experiments.

724 For delay epoch photoinactivation (**Fig. 1g-i** and **EDFig. 1b**), light was delivered at the onset of the delay epoch
725 and lasted for 0.6 s followed by a 0.2 s linear ramp down. We targeted one of three regions per session: bilateral
726 motor cortex (ALM and tjM1), bilateral ALM, or bilateral tjM1. A scanning galvo system (THORLABS GPS011)
727 was used to simultaneously target both hemispheres by scanning at 40 Hz. The beam (2 mm diameter) was centered
728 around the following locations: ALM (AP 2.5 mm, ML 1.5 mm), tjM1 (AP 1.75 mm, ML 2.25 mm), motor cortex
729 (i.e. ALM and tjM1; AP 2.25 mm, ML 1.85 mm). Due to their proximity, when specifically targeting ALM or tjM1,
730 Kwik-Cast™ (World Precision Instruments) was applied to the surrounding regions to prevent photoinactivation of
731 other regions. For photoinactivation at the go cue (**Fig. 1b,c** and **EDFig. 1c,d**), light was delivered to the motor
732 cortex for 0.8 s followed by a 0.2 s ramp down beginning at the go cue presentation.

733 *Electrophysiology recordings*
734 Extracellular recordings were performed in the ALM using one of two types of silicon probes: H2 probes, which
735 have two shanks, each with 32 channels with 25-µm spacing (Cambridge Neurotech) or Neuropixels 1.0[103] which
736 have one shank and allow recording from 384 channels arranged in a checkerboard pattern (IMEC). For recordings
737 with H2 probes, the 64-channel voltage signals were multiplexed using a Whisper recording system (Neural
738 Circuits, LLC), recorded on a PXI-8133 board (National Instruments) and digitized at 14 bits. The signals were
739 demultiplexed into 64 voltage traces sampled at 25 kHz and stored for offline analysis.

740 At least 6 hours before recording, a small craniotomy (1-1.5 mm diameter) was made over ALM (AP 2.5 mm, ML
741 1.5 mm). 2-5 recordings were performed on a single craniotomy on consecutive days. After inserting the probes
742 between 900 and 1100 µm (MPM System, New Scale Technologies), brain tissue was allowed to settle for at least
743 5   minutes   before   starting   recordings.   All   recordings   were   made   using   SpikeGLX
744 (https://github.com/billkarsh/SpikeGLX).

745 *Behavioral analysis*
746 All sessions used for behavioral analysis had at least 40 correct DR trials for each direction (left or right) and 20
747 correct WC trials for each direction, excluding early lick and ignore trials, which were omitted from all analyses.
748 To assess the impact of ALM photoinactivation on movement initiation, we first calculated the percent of trials with
749 a correct lick within 600 ms of the go cue/water drop (**Fig. 1c**). To find the fraction of time with the tongue visible
750 during the photoinactivation period (**EDFig. 1d**), for each trial we found the number of time-points within the 1 s
751 after the go cue/water drop where the tongue was labelled as visible by DeepLabCut and divided that by the total
752 number of time-points within the photoinactivation period. This was then averaged for all control or
753 photoinactivation trials for a given session.

754 To assess the impact of bilateral MC/ALM/tjM1 photoinactivation during the delay epoch, the average motion
755 energy during the delay epoch was calculated separately for right and left control vs. photoinactivation trials (**Fig.
756 1h** and **EDFig. 1b**).

757 *Electrophysiology recording analysis*
758 JRCLUST[104]   (https://github.com/JaneliaSciComp/JRCLUST)   and/or   Kilosort3[105]
759 (https://github.com/MouseLand/Kilosort) with manual curation using Phy (https://github.com/cortex-lab/phy) were
760 used for spike sorting. A unit was considered a well-isolated single unit based on manual inspection of its ISI
761 histogram, separation from other units, and its stationarity across the session[106]. Units that passed manual curation
762 but had a higher ISI violation rate were called multiunits. Recording sessions were only included for analysis if
763 they had at least 10 units (see **EDFig. 2** for a distribution of neuron counts across sessions). For the DR task, we
764 recorded 1651 units (483 single units) in ALM from 25 sessions using 9 mice. In 12 sessions from 6 mice, animals
765 performed the two-context task. 522 units (214 well-isolated single units) were recorded in these sessions. Finally,
766 for the randomized delay task, we recorded 845 units (288 well-isolated single units) in ALM from 19 sessions
767 using 4 mice. For subspace alignment (**Figs. 5g,n**, **7d,h**, and **Fig. 8d**) and single-unit selectivity analyses (**Fig. 3g**
768 and **EDFig. 4c**) only well-isolated single units with firing rates exceeding 1 Hz were included. All units with firing
769 rates exceeding 1 Hz were included in all other analyses.

770 To find choice-selective neurons, forty trials were subsampled for both right and left correct trials and a *ranksum*
771 test was used to compare spike counts for each unit during the sample, delay, or response epochs. Selective units

were those with significantly different spike counts ($p < 0.05$) during a given epoch. Context-selective units were defined in a two-step process to ensure that we were not conflating context selectivity with slow changes in animal engagement/motivation over each session. First, forty trials each were subsampled for DR and WC trials and spike counts were compared ($p < 0.05$, *ranksum* test) during the ITI (the 300 ms preceding the sample tone onset) when the animal received no external cues to indicate which context it was in. Because sessions always began with a DR block and often ended with a WC block, it is possible that differences in firing rates across contexts defined in this way could be representing time within the session. To account for this, for each unit identified in the first step, we calculated the difference in spike rate for each pair of DR and WC blocks (e.g. a session with five blocks, DR-WC-DR-WC-DR, would have nPairs=4 adjacent, overlapping block pairs) and included units as context-selective only if their *preferred* context (context with a higher spike rate) was the same for at least nPairs - 1 of the block pairs.

Selectivity in the neural population (**EDFig. 4c**) was calculated as the difference in spike rate on *preferred – non-preferred* trials in choice-selective units, with *preferred* trials referring to the trial type with a higher spike rate for each unit.

Coding direction analysis

Coding directions (CD) were defined as directions in neural activity state space, defined by firing rates, that maximally separated trajectories of two conditions.

CD$_{choice}$ and CD$_{action}$ were calculated as:

$$v = \frac{\overline{x}_{lickright} - \overline{x}_{lickleft}}{\sqrt{\mathrm{var}(x_{lickright}) + \mathrm{var}(x_{lickleft})}}$$

$$CD = \frac{v}{\sum |v|}$$

For each unit, the mean spike rate difference between right lick trials, $\overline{x}_{lickright}$, and left lick trials, $\overline{x}_{lickleft}$, was calculated in a 400 ms time interval. $\overline{x}_{lickright}$ and $\overline{x}_{lickleft}$ were then individually baseline subtracted and scaled by baseline standard deviation before calculating CDs (baseline: -2.4 to -2.2 seconds relative to the go cue, during the ITI). CD$_{choice}$ was calculated in the last 400 ms of the delay epoch and CD$_{action}$ was calculated in the first 400 ms of the response epoch. The vector v was then obtained by normalizing by the square root of the sum of the variances across conditions. Finally, v was normalized by its L$_1$ norm to ensure projections do not scale with the length of v, the number of units simultaneously recorded.

CD$_{ramp}$ was calculated as:

$$v = \frac{\overline{x}_{delay} - \overline{x}_{ITI}}{\sqrt{\mathrm{var}(x_{delay}) + \mathrm{var}(x_{ITI})}}$$

$$CD = \frac{v}{\sum |v|}$$

This calculation was similar to the calculations of CD$_{choice}$ and CD$_{action}$ but incorporated data from all correct DR trials during the last 400 ms of the delay epoch, $\overline{x}_{delay}$, and during the ITI (300 ms preceding the sample tone onset), $\overline{x}_{ITI}$. $\overline{x}_{delay}$ and $\overline{x}_{ITI}$ were both standardized using the baseline statistics from all correct DR trials.

To find CD$_{context}$, we first calculated a CD$_{context}{}^{p}$ for each pair, p, of DR and WC blocks in a session. If the session ended with a WC block, that block was excluded. CD$_{context}{}^{p}$ was calculated as:

$$v_p = \frac{\overline{x}_{DR^p} - \overline{x}_{WC^p}}{\sqrt{\mathrm{var}(x_{DR^p}) + \mathrm{var}(x_{WC^p})}}$$

814
815

$$CD_p = \frac{v_p}{\sum |v_p|}$$

816
817

818 $CD_{context}$ was then defined as the average over all $CD_{context}{}^p$ in a session. The calculation of $CD_{context}{}^p$ was similar
819 to the calculation of other CDs but incorporated data from the ITI of correct DR, $\overline{x}_{DR^p}$, and correct WC, $\overline{x}_{WC^p}$,
820 trials in a given pair of blocks. $\overline{x}_{DR^p}$ and $\overline{x}_{WC^p}$ were standardized using the baseline statistics from all correct DR
821 and WC trials.

822 CD_{action} was orthogonalized to CD_{choice} to exclusively capture response epoch selectivity that emerges after the go
823 cue. CD_{ramp} was orthogonalized to CD_{action} and CD_{choice} to remove selectivity that may emerge during the response
824 epoch that is also captured in CD_{action}. Orthogonalization was performed using the Gram-Schmidt process.

825 Projections of the population activity, $x \in \mathbb{R}^{(B*K) \times N}$ along the CD were calculated as:
826
827

$$proj = CD^T * x$$

828
829 where B is the number of time bins, K the number of trials, N the number of neurons, and T is the transpose operator.

830 For the randomized delay task, trials with non-1.2 s delay lengths were used to calculate CD_{choice} (fit trials), always
831 using the last 600 ms of the delay epoch as the time interval for calculation[65]. Population activity from trials with
832 1.2 s delays (test trials) were then projected along the CD_{choice} (**Fig. 3h,** *top left* and **Fig. 3i**, *middle*). For
833 visualization purposes, trials with all delay lengths (including fit trials) were projected along CD_{choice} in **Fig. 3i,**
834 *top*.

835 *Reliability of choice decoding from CD_{choice}*
836 An ROC-AUC analysis was performed to estimate the reliability of choice decoding from projections along CD_{choice}
837 on a single session basis (**EDFig. 2c**). For each session, equal numbers of correct left and rick lick trials were split
838 into a training (70%) and testing set (30%). CD_{choice} was calculated from the activity of the neural population using
839 training trials as described above. Activity from testing trials was projected along CD_{choice} and provided as input to
840 a logistic regression model (fitglm() in MATLAB with distribution='Binomial', link='logit'). The model was
841 optimized to predict the animal's choice on a particular trial from the delay epoch CD_{choice} activity. The model
842 output was then passed into MATLAB's perfcurve() function to obtain a receiver operating curve (ROC). Reliability
843 of decoding was measured as the area under the ROC (AUC), shown in the inset of **EDFig. 2c**.
844

845 *Choice/context decoding from neural population or kinematic features*
846 We trained logistic regression models to predict either animal choice (**Fig. 3b**) or behavioral context (**Fig. 4b**) from
847 either kinematic features or single trial neural activity. The kinematic regressors were made up of the x and y
848 positions and velocities of DeepLabCut-tracked features (tongue, jaw, and nose), as well as the tongue length, angle,
849 and motion energy. The neural regressors were the firing rates of the units simultaneously recorded within each
850 session. Equal numbers of correct left and right lick trials were used for this analysis. A separate model was trained
851 at each time bin for both neural and kinematic decoding. Models were trained with ridge regularization and 4-fold
852 cross-validation with 30% of trials held out for testing. Chance accuracy was obtained by shuffling choice/context
853 labels across trials. Accuracy of the prediction was defined as:
854

$$Accuracy = \frac{Number\ of\ correct\ predictions}{Total\ number\ of\ predictions}$$

856

857 *Emergence of CD_{choice} selectivity/motion energy in randomized vs. fixed delay tasks*
858 To find selectivity within the CD_{choice} projection (**Fig. 3h,** *top left*) we found the difference between the trial-
859 averaged projection on right and left trials for each session. We then found the maximum selectivity value prior to
860 the go cue and identified the first time point, relative to delay onset, for the selectivity trace to exceed 90% of the

861   maximum value (**Fig. 3h,** *top right*). The same metric was found using session-averaged motion energy in **Fig. 3h,**
862   *bottom panels*.
863

864   *Predicting projections along coding directions from kinematic features*
865   We trained support vector machines (SVMs) to predict projections along CD_{choice}, CD_{ramp}, and $CD_{context}$. Correct
866   DR trials were used for predicting CD_{choice} and CD_{ramp} projections; correct DR and WC trials were used for
867   predicting $CD_{context}$. For predicting $CD_{context}$, the regressors were made up of the x and y positions and velocities
868   of DeepLabCut-tracked features (multiple points on the tongue, jaw, and nose taken from two camera angles), as
869   well as the tongue length, angle, and motion energy (totaling 60 regressors). Only the sample and delay epoch were
870   considered when predicting CD_{choice} and CD_{ramp} projections; because of this, any tongue-related metrics were not
871   included as regressors in these analyses (totaling 55 regressors). Projections and kinematic features were first mean-
872   centered and scaled to unit variance before input to the regression model. The previous B time bins of kinematic
873   data were used to predict the current bin's neural data (B=6, each bin is 5 ms). Models were trained with ridge
874   regularization and 4-fold cross-validation. The models were tested on held-out testing data (40% of trials for
875   CD_{choice} and CD_{ramp}; tested on 30% of trials for $CD_{context}$). To assess the prediction quality between projections and
876   model predictions, we calculated the variance explained as:
877

878
$$R^2 = 1 - \frac{\sum_t(y_t - \hat{y}_t)^2}{\sum_t(y_t - \overline{y})^2}$$

879
880   where y_i is the value of the projection at time *t*, $\hat{y}_t$ is the prediction, and $\overline{y}$ is the mean of the projection across all
881   time.

882   When predicting projections along CD_{choice} during the randomized delay task, unregularized models were used
883   (**Fig. 3h**). This was due to the small numbers of trials for each delay length which precluded the partitioning of data
884   into 3 separate sets (training, validation, and testing trials). Instead, models were trained with linear regression and
885   4-fold cross-validation and tested on held-out data from each cross-validation fold. For assessing prediction quality
886   between projections and model predictions, trials with 1.2 s delay epochs were used.

887   To understand which groups of kinematic features were most informative for predicting projections along CD_{choice},
888   or $CD_{context}$ (**EDFig. 3**), the absolute value of the beta coefficients for each kinematic regressor in the trained model
889   was first obtained. For each feature group (jaw, nose, motion energy), the average beta coefficient across all
890   regressors belonging to this kinematic feature group (8*B for jaw, 6*B for nose, and 1*B for motion energy; for
891   example, the x and y positions and velocities for one point on the jaw on each camera totals 8 jaw regressors for
892   each time bin, B) was calculated. The average beta coefficient for each feature group was then expressed as a
893   fraction of the total of all beta coefficients.

894   *Subspace identification (trial-averaged data)*
895   Delay and Response subspaces were identified following the general approach described in ref[40]. For identifying
896   subspaces using trial-averaged data (**Fig. 5a**), neural activity was first trial-averaged separately for correct left and
897   right trials. Activity across trial types was then concatenated, to produce a matrix $X \in \mathbb{R}^{(B*C) \times N}$, where B is the
898   number of time bins, C the number of trial types, and N the number of units. Trial-averaged neural activity was
899   soft-normalized (normalization factor=5) as described in ref[40] and subsequently baseline subtracted (baseline: -2.4
900   to -2.2 s before go cue, during the ITI) The matrix, *X*, was further divided into two matrices, X_{delay} and $X_{response}$. X_{delay}
901   contained activity from [-1,0] seconds relative to the go cue, and $X_{response}$ contained activity from [0,1] seconds
902   relative to the go cue. Delay and response subspaces were then identified by solving the following optimization
903   problem:
904

905
$$[\widehat{Q}_{delay}, \widehat{Q}_{response}]$$

906
$$= argmax_{[Q_{delay}, Q_{response}]} \frac{1}{2} \frac{Tr(Q_{delay}^T C_{delay} Q_{delay})}{\sum_{i=1}^{d_{delay}} \sigma_{delay}(i)} + \frac{1}{2} \frac{Tr(Q_{response}^T C_{response} Q_{response})}{\sum_{i=1}^{d_{response}} \sigma_{response}(i)}$$

907
908
$$subject\ to\ \ Q_{delay}^T Q_{response} = 0, \qquad Q_{delay}^T Q_{delay} = I, \qquad Q_{response}^T Q_{response} = I$$

909
910
911 where C_{delay} and $C_{response}$ are the covariances of X_{delay} and $X_{response}$, σ_{delay} and $\sigma_{response}$ are the singular values of
912 C_{delay} and $C_{response}$, and d_{delay} and $d_{response}$ are the dimensionality of the subspaces. This optimization problem jointly
913 identifies the subspaces that maximally contain the variance in neural activity during the delay and response epochs.
914 The dimensionality of each space was chosen to be half the number of simultaneously recorded neurons, or twenty,
915 whichever was smaller. Therefore, the dimensionality of the full population was equal to the dimensionality of the
916 delay or response subspaces for sessions containing forty or fewer neurons. Optimization was performed using the
917 manopt[107] toolbox for MATLAB.

918 *Subspace identification (single-trial data)*
919 For identifying subspaces using single-trial data (**Fig 5h**), single-trial neural activity was first binned in 5 ms
920 intervals and smoothed with a causal Gaussian kernel with a half width of 35 ms. Each trial's activity was subtracted
921 by the average baseline activity across trials and scaled by the standard deviation across trials (baseline: -2.4 to -2.2
922 s before go cue, during the ITI). $\mathbf{X}_{moving} \in \mathbb{R}^{B\_P \times N}$ and $\mathbf{X}_{stationary} \in \mathbb{R}^{B\_n \times N}$ were defined using the single trial neural
923 activity when the animal was moving or stationary (see ***Motion Energy***), respectively. B_n was the number of time
924 bins during which the animal was annotated as stationary and B_p the number of time points annotated as moving.
925 All correct and error trials from DR and WC contexts were used unless specified otherwise. Once the data was
926 partitioned into moving and stationary time points, subspace identification was carried as described for trial-
927 averaged data in the preceding paragraph:

928
929
$$[\widehat{Q}_{mov-null}, \widehat{Q}_{mov-pot}]$$

930
$$= argmax_{[Q_{mov-null}, Q_{mov-pot}]} \frac{1}{2} \frac{Tr(Q_{mov-null}^T C_{stationary} Q_{mov-null})}{\sum_{i=1}^{d_{mov-null}} \sigma_{stationary}(i)}$$

931
$$+ \frac{1}{2} \frac{Tr(Q_{mov-pot}^T C_{moving} Q_{mov-pot})}{\sum_{i=1}^{d_{mov-pot}} \sigma_{moving}(i)}$$

932
933 $$subject\ to\ \ Q_{mov-null}^T Q_{mov-pot} = 0, \qquad Q_{mov-null}^T Q_{mov-null} = I, \qquad Q_{mov-pot}^T Q_{mov-pot} = I$$

934
935 We quantified the normalized variance explained in a subspace as in refs[40,108] (**Fig. 5d,k**):

936
937
$$normVE = \frac{Tr(Q^T C Q)}{\sum_{i=1}^{d} \sigma(i)}$$

938
939 where $\mathbf{Q}$ is the subspace, $\mathbf{C}$ is the covariance of neural activity, and σ are the singular values of $\mathbf{C}$. This normalization
940 provides the maximum variance that can be captured by d dimensions.

941 Unit activity was reconstructed from movement-null and movement-potent subspaces according to the following
942 equation:
943
$$X_{subspace} = X Q^T$$

944
945
$$X_{recon} = X_{subspace} Q$$

946
947 where X_{recon} is the reconstructed neural activity, $X_{subspace}$ is the projected neural activity within the movement-null
948 or movement-potent subspace, X is either single-trial or trial-averaged firing rates and Q is either the movement-
949 null or movement-potent subspace.

950 Bootstrapped distributions of coding directions within the movement-null and movement-potent subspaces were
951 obtained through two separate methods. For **Fig. 7** and **EDFig. 7a,c**, we first estimated movement-null and
952 movement-potent subspaces per session and reconstructed neural activity from each subspace. Then, we performed
953 the hierarchical bootstrapping procedure as described in ***Hierarchical bootstrapping***. For each iteration, we used
954 the original neural activity to estimate the coding directions and then projected the reconstructed neural activity

955 onto the coding directions. For **EDFig. 5b**, for each bootstrap iteration, the reconstructed neural activity itself was
956 used to estimate the coding directions. Activity within each subspace was then projected along the respective coding
957 directions. For **Fig. 7b,f**, coding directions were directly identified from the reconstructed neural activity, $\mathbf{X}_{recon}$, for
958 the individual example sessions.

959 Subspace alignment for an individual unit was calculated as:

$$A = \frac{VE_{mov-null} - VE_{mov-pot}}{VE_{mov-null} + VE_{mov-pot}}$$

963 where VE is the variance explained of each individual unit by the movement-null or movement-potent subspace, or
964 by the activity along a coding direction within the movement-null or movement-potent subspace. VE for a single
965 unit was calculated as:

$$VE = 1 - \frac{\sum_t (x_t - \hat{x}_t)^2}{\sum_t (x_t - \bar{x})^2}$$

969 where x_t is the trial-averaged firing rate, $\hat{x}$ is the reconstructed trial-averaged firing rate, and t is the time bin.

970 To ask if the number of single units observed to be aligned to either the movement-null or movement-potent
971 subspace was different than expected by chance, we compared the distributions to those obtained from randomly
972 sampled subspaces as described in ref[40]. Each element comprising a subspace was randomly sampled from a normal
973 distribution with zero mean and unit variance but was biased by the covariance structure of the neural activity for a
974 given session. Biasing the randomly sampled subspaces by the covariances controls for the unbalanced variance
975 between stationary and moving time points (or between delay and response epochs). That is to say that the shuffled
976 distributions take into account the relative amount of movement tuning across the neural population.

977 We sampled random subspaces, $v_{mov\text{-}null}$ and $v_{mov\text{-}pot}$ as follows:

$$v_{mov-null} = orth\left(\frac{U_{mov-null}\sqrt{S_{mov-null}}v}{\left\|U_{mov-null}\sqrt{S_{mov-null}}v\right\|_2}\right)$$

$$v_{mov-potent} = orth\left(\frac{U_{mov-pot}\sqrt{S_{mov-pot}}v}{\left\|U_{mov-pot}\sqrt{S_{mov-pot}}v\right\|_2}\right)$$

980 Where $\mathbf{U}$ and $\mathbf{S}$ are the left and right singular vectors of their associated covariance matrices, $\mathbf{C}_{stationary}$ and $\mathbf{C}_{moving}$,
981 and v is a matrix whose elements are independently drawn from a normal distribution with zero mean and unit
982 variance. As described above, covariance matrices $\mathbf{C}_{stationary}$ and $\mathbf{C}_{moving}$ are defined by neural activity during
983 stationary and movement time points for single trial data. $orth(\mathbf{A})$ computes the orthonormal basis of a matrix $\mathbf{A}$.
984 Neural activity from each session was projected along the randomly sampled subspaces and alignment indices were
985 calculated. This procedure was repeated 1000 times to generate null distributions, which represents the alignment
986 indices of our data with random subspaces (**EDFig. 5**). To generate p-values associated with **Fig. 5n**, **Fig. 7d,h**,
987 **and Fig. 8d**, on each iteration, we computed the proportion of strongly tuned units (alignment ≥ 0.8 and alignment
988 ≤ -0.8). This provided two distributions, one for alignment ≥ 0.8 and another for alignment ≤ -0.8. These chance
989 distributions were separately fit with gaussian distributions using the fitgmdist() function in MATLAB. Then, p-
990 values were computed as the probability of observing the proportion of tuned units we observe in the data from the
991 fitted distributions.

992 Subspaces were identified using data from DR and WC correct and error trials (**Fig. 5,7,** and **8**). Control analyses
993 were performed using separate sets of trials to assess if the movement-potent subspace erroneously contained
994 movement-null-subspace dynamics. First, we estimated subspaces using WC trials only (**EDFigs. 4** and **8**). Second,
995 we estimated subspaces using DR and WC trials, but restricted time points used to those in the response epoch only
996 (**EDFigs. 4** and **8**). Both controls allowed us to estimate movement-null and movement-potent subspaces in the
997 presence of uninstructed movements, but in the absence of planning dynamics. These controls thus allowed us to
998 measure the degree to which the movement-potent subspace erroneously captured movement-null dynamics.

In a further attempt to validate that the movement-potent subspace is not inadvertently capturing movement-correlated internal dynamics, we identified movement-null and movement-potent subspaces using a two-stage PCA approach (**EDFig. 4**). The movement-null subspace was first identified as the dominant principal components (first 5 PCs) of the single-trial firing rates when mice are not moving. Second, the activity within the movement-null subspace was removed from single-trial firing rates. Then, the movement-potent subspace was calculated as the first 5 PCs of the single-trial residuals:

$$X_{mov-null} = XQ_{mov-null}^{T}$$

$$X_{recon,mov-null} = X_{mov-null}Q_{mov-null}$$

$$Q_{mov-pot} = PCA(X - X_{recon,mov-null})$$

$$X_{mov-pot} = XQ_{mov-pot}^{T}$$

$X \in \mathbb{R}^{(B*K) \times N}$ is the single-trial firing rates where B is the number of time points, K the number of trials, and N the number of units. $Q_{mov-null}$ is the first 5 PCs of the single-trial firing rates when animals are stationary, and $X_{mov-null}$ is the projection along those PCs. $X_{recon,mov-null}$ is the reconstructed neural activity obtained from the multiplication of activity within the movement-null subspace, $X_{mov-null}$, and the movement-null subspace, $Q_{mov-null}$. $PCA(Z)$ indicates computing the PCs of the matrix Z. $Q_{mov-pot}$ is the first 5 PCs of the single-trial residuals obtained from subtracting $X_{mov-null}$ from the single-trial firing rates, X. Finally, $X_{mov-pot}$ is obtained from projecting single-trial firing rates onto $Q_{mov-pot}$. $X_{recon,mov-null}$ contains activity that is explainable by the first 5 PCs in the absence of movement and, therefore, the residuals contain movement-related neural dynamics. Thus, performing PCA on these residuals provides a movement-potent subspace that is orthogonal to the movement-null subspace. This approach ensures dynamics observed during stationarity are contained within the movement-null subspace prior to assigning any dynamics to the movement-potent subspace. Therefore, it is more conservative in avoiding the mis-assignment of movement-correlated internal dynamics to the movement-potent subspace.

CD$_{context}$ selectivity on 'High move' and 'Low move' trials
For each session, DR and WC trials were first separated into 'High move' and 'Low move' trials. 'High move' trials were those where the average motion energy in the ITI was greater than the movement threshold for that session (see ***Motion energy***). 'Low move' trials were the remaining trials. The last 40 trials in each session were excluded from analysis to account for the decrease in uninstructed movements that are observed towards the end of behavioral sessions as animals become sated and disengaged. CD$_{context}$ was calculated from the full population or from neural activity reconstructed from either subspace. Population activity from 'High-move' and 'Low-move' trials was then projected along CD$_{context}$. Selectivity was defined as the trial-averaged projection along CD$_{context}$ on DR trials minus the projection along CD$_{context}$ on WC trials (**Fig. 8b,c**).

Hierarchical bootstrapping
Projections along coding directions were obtained via a hierarchical bootstrapping procedure[109,110] (**Figs. 2, 7** and **EDFigs. 7, 8** and **10**). Pseudopopulations were constructed by randomly sampling with replacement M mice, 2 sessions per sampled mouse, 50 correct trials of each type, 20 error trials of each type, and 20 neurons. M is the number of mice in the original cohort. Bootstrapping was repeated for 1000 iterations. In each iteration, data derived from some individual mice (and sessions, trials, and neurons) will be overrepresented and some will be omitted. Average effects driven by small subsets of animals, sessions, trials, and/or units will be accompanied by large confidence intervals. For all results obtained through this bootstrapping procedure, mean and 95% confidence intervals (shaded area) of the bootstrap distribution are shown, except for selectivity (**Fig. 7a** and **EDFig. 7a**), where 5-95% confidence intervals are shown to indicate where projections significantly differ from zero ($p < 0.05$, one-sided test, bootstrap).

Statistics
No statistical methods were used to determine sample sizes. All t-tests were two-sided unless stated otherwise.

References

1. Alexander, G. E. & Crutcher, M. D. Neural representations of the target (goal) of visually guided arm movements in three motor areas of the monkey. *Journal of Neurophysiology* **64**, 164–178 (1990).

2. Cisek, P. & Kalaska, J. F. Neural Correlates of Reaching Decisions in Dorsal Premotor Cortex: Specification of Multiple Direction Choices and Final Selection of Action. *Neuron* **45**, 801–814 (2005).

3. Lebedev, M. A. & Wise, S. P. Insights into Seeing and Grasping: Distinguishing the Neural Correlates of Perception and Action. *Behavioral and Cognitive Neuroscience Reviews* **1**, 108–129 (2002).

4. Chandrasekaran, C., Peixoto, D., Newsome, W. T. & Shenoy, K. V. Laminar differences in decision-related neural activity in dorsal premotor cortex. *Nat Commun* **8**, 614 (2017).

5. Chen, S. *et al.* Brain-wide neural activity underlying memory-guided movement. *Cell* **187**, 676-691.e16 (2024).

6. Basso, M. A. & May, P. J. Circuits for Action and Cognition: A View from the Superior Colliculus. *Annu Rev Vis Sci* **3**, 197–226 (2017).

1082   7.   Zimnik, A. J. & Churchland, M. M. Independent generation of sequence elements by motor cortex.

1083   *Nat Neurosci* **24**, 412–424 (2021).

1084   8.   Ames, K. C., Ryu, S. I. & Shenoy, K. V. Simultaneous motor preparation and execution in a last-

1085   moment reach correction task. *Nat Commun* **10**, 2718 (2019).

1086   9.   Flash, T. & Henis, E. Arm Trajectory Modifications During Reaching Towards Visual Targets.

1087   *Journal of Cognitive Neuroscience* **3**, 220–230 (1991).

1088   10. Fuster, J. M. & Alexander, G. E. Neuron activity related to short-term memory. *Science* **173**, 652–

1089   654 (1971).

1090   11. Romo, R., Brody, C. D., Hernández, A. & Lemus, L. Neuronal correlates of parametric working

1091   memory in the prefrontal cortex. *Nature* **399**, 470–473 (1999).

1092   12. Erlich, J. C., Bialek, M. & Brody, C. D. A Cortical Substrate for Memory-Guided Orienting in the

1093   Rat. *Neuron* **72**, 330–343 (2011).

1094   13. Tanji, J. & Evarts, E. V. Anticipatory activity of motor cortex neurons in relation to direction of an

1095   intended movement. *Journal of Neurophysiology* **39**, 1062–1068 (1976).

1096   14. Guo, Z. V. *et al.* Flow of Cortical Activity Underlying a Tactile Decision in Mice. *Neuron* **81**, 179–

1097   194 (2014).

1098   15. Wallis, J. D., Anderson, K. C. & Miller, E. K. Single neurons in prefrontal cortex encode abstract

1099   rules. *Nature* **411**, 953–956 (2001).

1100   16. Mante, V., Sussillo, D., Shenoy, K. V. & Newsome, W. T. Context-dependent computation by

1101   recurrent dynamics in prefrontal cortex. *Nature* **503**, 78–84 (2013).

1102   17. Schultz, W., Dayan, P. & Montague, P. R. A Neural Substrate of Prediction and Reward. *Science*

1103   **275**, 1593–1599 (1997).

1104   18. Watabe-Uchida, M., Eshel, N. & Uchida, N. Neural Circuitry of Reward Prediction Error. *Annual*

1105   *Review of Neuroscience* **40**, 373–394 (2017).

1106   19. Freedman, D. J., Riesenhuber, M., Poggio, T. & Miller, E. K. Categorical representation of visual

1107   stimuli in the primate prefrontal cortex. *Science* **291**, 312–316 (2001).

1108   20.   Carr, M. F., Jadhav, S. P. & Frank, L. M. Hippocampal replay in the awake state: a potential

1109   substrate for memory consolidation and retrieval. *Nat Neurosci* **14**, 147–153 (2011).

1110   21.   Levy, S. *et al.* Cell-Type-Specific Outcome Representation in the Primary Motor Cortex. *Neuron*

1111   **107**, 954-971.e9 (2020).

1112   22.   Padoa-Schioppa, C. & Assad, J. A. Neurons in Orbitofrontal Cortex Encode Economic Value.

1113   *Nature* **441**, 223–226 (2006).

1114   23.   Zagha, E. The Importance of Accounting for Movement When Relating Neuronal Activity to

1115   Sensory and Cognitive Processes | Journal of Neuroscience.

1116   https://www.jneurosci.org/content/42/8/1375#ref-90 (2022).

1117   24.   Drew, P. J., Winder, A. T. & Zhang, Q. Twitches, Blinks, and Fidgets: Important Generators of

1118   Ongoing Neural Activity. *Neuroscientist* **25**, 298–313 (2019).

1119   25.   Galton, F. The Measure of Fidget. *Nature* **32**, 174–175 (1885).

1120   26.   Hulsey, D., Zumwalt, K., Mazzucato, L., McCormick, D. A. & Jaramillo, S. Decision-making

1121   dynamics are predicted by arousal and uninstructed movements. *Cell Reports* **43**, 113709 (2024).

1122   27.   Tremblay, S., Testard, C., DiTullio, R. W., Inchauspé, J. & Petrides, M. Neural cognitive signals

1123   during spontaneous movements in the macaque. *Nat Neurosci* **26**, 295–305 (2023).

1124   28.   Hafed, Z. M., Lovejoy, L. P. & Krauzlis, R. J. Modulation of Microsaccades in Monkey during a

1125   Covert Visual Attention Task. *J Neurosci* **31**, 15219–15230 (2011).

1126   29.   Corneil, B. D., Munoz, D. P., Chapman, B. B., Admans, T. & Cushing, S. L. Neuromuscular

1127   consequences of reflexive covert orienting. *Nat Neurosci* **11**, 13–15 (2008).

1128   30.   Musall, S., Kaufman, M. T., Juavinett, A. L., Gluf, S. & Churchland, A. K. Single-trial neural

1129   dynamics are dominated by richly varied movements. *Nat Neurosci* **22**, 1677–1686 (2019).

1130   31.   Stringer, C. Spontaneous behaviors drive multidimensional, brainwide activity | Science.

1131   https://www.science.org/doi/10.1126/science.aav7893 (2019).

1132   32.   Steinmetz, N. A., Zatka-Haas, P., Carandini, M. & Harris, K. D. Distributed coding of choice, action

1133   and engagement across the mouse brain. *Nature* **576**, 266–273 (2019).

1134 33. Mangin, E. N., Chen, J., Lin, J. & Li, N. Behavioral measurements of motor readiness in mice.

1135 *Current Biology* **33**, 3610-3624.e4 (2023).

1136 34. Terada, S.-I., Kobayashi, K. & Matsuzaki, M. Transition of distinct context-dependent ensembles

1137 from secondary to primary motor cortex in skilled motor performance. *Cell Reports* **41**, 111494

1138 (2022).

1139 35. Lowet, E. *et al.* Enhanced Neural Processing by Covert Attention only during Microsaccades

1140 Directed toward the Attended Stimulus. *Neuron* **99**, 207-214.e3 (2018).

1141 36. Popescu, S. T. & Wexler, M. Spontaneous Body Movements in Spatial Cognition. *Front Psychol* **3**,

1142 136 (2012).

1143 37. Hajnal, J. V. *et al.* Artifacts due to stimulus correlated motion in functional imaging of the brain.

1144 *Magn Reson Med* **31**, 283–291 (1994).

1145 38. Dominiak, S. E. *et al.* Whisking Asymmetry Signals Motor Preparation and the Behavioral State of

1146 Mice. *J. Neurosci.* **39**, 9818–9830 (2019).

1147 39. Kaufman, M. T., Churchland, M. M., Ryu, S. I. & Shenoy, K. V. Cortical activity in the null space:

1148 permitting preparation without movement. *Nat Neurosci* **17**, 440–448 (2014).

1149 40. Elsayed, G. F., Lara, A. H., Kaufman, M. T., Churchland, M. M. & Cunningham, J. P.

1150 Reorganization between preparatory and movement population responses in motor cortex. *Nat*

1151 *Commun* **7**, 13239 (2016).

1152 41. Liu, T. T., Nalci, A. & Falahpour, M. The global signal in fMRI: Nuisance or Information?

1153 *NeuroImage* **150**, 213–229 (2017).

1154 42. Friston, K. J., Williams, S., Howard, R., Frackowiak, R. S. J. & Turner, R. Movement-Related

1155 effects in fMRI time-series. *Magnetic Resonance in Medicine* **35**, 346–355 (1996).

1156 43. Bullmore, E. T. *et al.* Methods for diagnosis and treatment of stimulus-correlated motion in generic

1157 brain activation studies using fMRI. *Hum Brain Mapp* **7**, 38–48 (1998).

1158 44. Power, J. D., Schlaggar, B. L. & Petersen, S. E. Recent progress and outstanding issues in motion

1159 correction in resting state fMRI. *NeuroImage* **0**, 536 (2015).

1160 45. Cisek, P. & Kalaska, J. F. Neural Mechanisms for Interacting with a World Full of Action Choices.

1161   *Annual Review of Neuroscience* **33**, 269–298 (2010).

1162 46. Cisek, P. & Pastor-Bernier, A. On the challenges and mechanisms of embodied decisions.

1163   *Philosophical Transactions of the Royal Society B: Biological Sciences* **369**, 20130479 (2014).

1164 47. Koay, S. A., Charles, A. S., Thiberge, S. Y., Brody, C. D. & Tank, D. W. Sequential and efficient

1165   neural-population coding of complex task information. *Neuron* **110**, 328-349.e11 (2022).

1166 48. Aoi, M. C., Mante, V. & Pillow, J. W. Prefrontal cortex exhibits multidimensional dynamic encoding

1167   during decision-making. *Nat Neurosci* **23**, 1410–1420 (2020).

1168 49. Hennig, J. A. *et al.* Learning is shaped by abrupt changes in neural engagement. *Nat Neurosci* **24**,

1169   727–736 (2021).

1170 50. Druckmann, S. & Chklovskii, D. B. Neuronal Circuits Underlying Persistent Representations

1171   Despite Time Varying Activity. *Current Biology* **22**, 2095–2103 (2012).

1172 51. Galiñanes, G. L., Bonardi, C. & Huber, D. Directional Reaching for Water as a Cortex-Dependent

1173   Behavioral Framework for Mice. *Cell Reports* **22**, 2767–2783 (2018).

1174 52. Mathis, A. *et al.* DeepLabCut: markerless pose estimation of user-defined body parts with deep

1175   learning. *Nat Neurosci* **21**, 1281–1289 (2018).

1176 53. Mayrhofer, J. M. *et al.* Distinct Contributions of Whisker Sensory Cortex and Tongue-Jaw Motor

1177   Cortex in a Goal-Directed Sensorimotor Transformation. *Neuron* **103**, 1034-1043.e5 (2019).

1178 54. Inagaki, H. K. *et al.* Neural Algorithms and Circuits for Motor Planning. *Annual Review of*

1179   *Neuroscience* **45**, 249–271 (2022).

1180 55. Xu, D. *et al.* Cortical processing of flexible and context-dependent sensorimotor sequences.

1181   *Nature* **603**, 464–469 (2022).

1182 56. Chen, T.-W., Li, N., Daie, K. & Svoboda, K. A Map of Anticipatory Activity in Mouse Motor Cortex.

1183   *Neuron* **94**, 866-879.e4 (2017).

1184 57. Yin, X., Wang, Y., Li, J. & Guo, Z. V. Lateralization of short-term memory in the frontal cortex. *Cell*

1185   *Reports* **40**, 111190 (2022).

1186   58.   Li, N., Chen, T.-W., Guo, Z. V., Gerfen, C. R. & Svoboda, K. A motor cortex circuit for motor

1187   planning and movement. *Nature* **519**, 51–56 (2015).

1188   59.   Esmaeili, V. *et al.* Rapid suppression and sustained activation of distinct cortical regions for a

1189   delayed sensory-triggered motor response. *Neuron* **109**, 2183-2201.e9 (2021).

1190   60.   Shenoy, K. V., Sahani, M. & Churchland, M. M. Cortical Control of Arm Movements: A Dynamical

1191   Systems Perspective. *Annual Review of Neuroscience* **36**, 337–359 (2013).

1192   61.   Li, N., Daie, K., Svoboda, K. & Druckmann, S. Robust neuronal dynamics in premotor cortex

1193   during motor planning. *Nature* **532**, 459–464 (2016).

1194   62.   Yang, W., Tipparaju, S. L., Chen, G. & Li, N. Thalamus-driven functional populations in frontal

1195   cortex support decision-making. *Nat Neurosci* **25**, 1339–1352 (2022).

1196   63.   Economo, M. N. *et al.* Distinct descending motor cortex pathways and their roles in movement.

1197   *Nature* **563**, 79–84 (2018).

1198   64.   Svoboda, K. & Li, N. Neural mechanisms of movement planning: motor cortex and beyond.

1199   *Current Opinion in Neurobiology* **49**, 33–41 (2018).

1200   65.   Inagaki, H. K., Fontolan, L., Romani, S. & Svoboda, K. Discrete attractor dynamics underlies

1201   persistent activity in the frontal cortex. *Nature* **566**, 212–217 (2019).

1202   66.   Orlandi, J. G., Abdolrahmani, M., Aoki, R., Lyamzin, D. R. & Benucci, A. Distributed context-

1203   dependent choice information in mouse posterior cortex. *Nat Commun* **14**, 192 (2023).

1204   67.   Inagaki, H. K., Inagaki, M., Romani, S. & Svoboda, K. Low-Dimensional and Monotonic

1205   Preparatory Activity in Mouse Anterior Lateral Motor Cortex. *J. Neurosci.* **38**, 4163–4185 (2018).

1206   68.   Finkelstein, A. *et al.* Attractor dynamics gate cortical information flow during decision-making. *Nat

1207   Neurosci* **24**, 843–850 (2021).

1208   69.   Narayanan, N. S. Ramping activity is a cortical mechanism of temporal control of action. *Current

1209   Opinion in Behavioral Sciences* **8**, 226–230 (2016).

1210   70.   Cisek, P., Puskas, G. A. & El-Murr, S. Decisions in Changing Conditions: The Urgency-Gating

1211   Model. *J. Neurosci.* **29**, 11560–11571 (2009).

71. Tanaka, M. Cognitive Signals in the Primate Motor Thalamus Predict Saccade Timing. *J. Neurosci.* **27**, 12109–12118 (2007).

72. Maimon, G. & Assad, J. A. A cognitive signal for the proactive timing of action in macaque LIP. *Nat Neurosci* **9**, 948–955 (2006).

73. Wang, Z. A. *et al.* Not everything, not everywhere, not all at once: a study of brain-wide encoding of movement. 2023.06.08.544257 Preprint at https://doi.org/10.1101/2023.06.08.544257 (2023).

74. Kawai, R. *et al.* Motor cortex is required for learning but not for executing a motor skill. *Neuron* **86**, 800–812 (2015).

75. Safaie, M. *et al.* Turning the body into a clock: Accurate timing is facilitated by simple stereotyped interactions with the environment. *Proceedings of the National Academy of Sciences* **117**, 13084–13093 (2020).

76. Chen, S. *et al.* Brain-wide neural activity underlying memory-guided movement. 2023.03.01.530520 Preprint at https://doi.org/10.1101/2023.03.01.530520 (2023).

77. Moore, J. D., Kleinfeld, D. & Wang, F. How the brainstem controls orofacial behaviors comprised of rhythmic actions. *Trends in Neurosciences* **37**, 370–380 (2014).

78. Arber, S. & Costa, R. M. Networking brainstem and basal ganglia circuits for movement. *Nat Rev Neurosci* **23**, 342–360 (2022).

79. Merel, J., Botvinick, M. & Wayne, G. Hierarchical motor control in mammals and machines. *Nat Commun* **10**, 5489 (2019).

80. Hausmann, S. B., Vargas, A. M., Mathis, A. & Mathis, M. W. Measuring and modeling the motor system with machine learning. *Current Opinion in Neurobiology* **70**, 11–23 (2021).

81. Pereira, T. D., Shaevitz, J. W. & Murthy, M. Quantifying behavior to understand the brain. *Nat Neurosci* **23**, 1537–1549 (2020).

82. Anderson, D. J. & Perona, P. Toward a Science of Computational Ethology. *Neuron* **84**, 18–31 (2014).

83. Miller, C. T. *et al.* Natural behavior is the language of the brain. *Current Biology* **32**, R482–R493 (2022).

1239 84. Krakauer, J. W., Ghazanfar, A. A., Gomez-Marin, A., MacIver, M. A. & Poeppel, D. Neuroscience

1240   Needs Behavior: Correcting a Reductionist Bias. *Neuron* **93**, 480–490 (2017).

1241 85. Datta, S. R., Anderson, D. J., Branson, K., Perona, P. & Leifer, A. Computational Neuroethology:

1242   A Call to Action. *Neuron* **104**, 11–24 (2019).

1243 86. Parker, P. R. L., Brown, M. A., Smear, M. C. & Niell, C. M. Movement-Related Signals in Sensory

1244   Areas: Roles in Natural Behavior. *Trends in Neurosciences* **43**, 581–595 (2020).

1245 87. Gomez-Marin, A. & Ghazanfar, A. A. The Life of Behavior. *Neuron* **104**, 25–36 (2019).

1246 88. Dennis, E. J. *et al.* Systems Neuroscience of Natural Behaviors in Rodents. *J. Neurosci.* **41**, 911–

1247   919 (2021).

1248 89. Testard, C. *et al.* Neural signatures of natural behavior in socializing macaques.

1249   2023.07.05.547833 Preprint at https://doi.org/10.1101/2023.07.05.547833 (2023).

1250 90. Marshall, J. D. *et al.* Continuous Whole-Body 3D Kinematic Recordings across the Rodent

1251   Behavioral Repertoire. *Neuron* **109**, 420-437.e8 (2021).

1252 91. Christensen, A. J., Ott, T. & Kepecs, A. Cognition and the single neuron: How cell types construct

1253   the dynamic computations of frontal cortex. *Current Opinion in Neurobiology* **77**, 102630 (2022).

1254 92. Gallego, J. A., Perich, M. G., Miller, L. E. & Solla, S. A. Neural Manifolds for the Control of

1255   Movement. *Neuron* **94**, 978–984 (2017).

1256 93. Fortunato, C. *et al.* Nonlinear manifolds underlie neural population activity during behaviour.

1257   2023.07.18.549575 Preprint at https://doi.org/10.1101/2023.07.18.549575 (2023).

1258 94. Dahmen, D. *et al.* Strong and localized recurrence controls dimensionality of neural activity across

1259   brain areas. 2020.11.02.365072 Preprint at https://doi.org/10.1101/2020.11.02.365072 (2023).

1260 95. Morales-Gregorio, A. *et al.* Neural manifolds in V1 change with top-down signals from V4 targeting

1261   the foveal region. 2023.06.14.544966 Preprint at https://doi.org/10.1101/2023.06.14.544966

1262   (2023).

1263 96. Sohn, H., Narain, D., Meirhaeghe, N. & Jazayeri, M. Bayesian Computation through Cortical

1264   Latent Dynamics. *Neuron* **103**, 934-947.e5 (2019).

97. Joshi, S. & Gold, J. I. Pupil Size as a Window on Neural Substrates of Cognition. *Trends in Cognitive Sciences* **24**, 466–480 (2020).

98. Lee, C. R. & Margolis, D. J. Pupil Dynamics Reflect Behavioral Choice and Learning in a Go/NoGo Tactile Decision-Making Task in Mice. *Frontiers in Behavioral Neuroscience* **10**, (2016).

99. Bradley, M. M., Miccoli, L., Escrig, M. A. & Lang, P. J. The pupil as a measure of emotional arousal and autonomic activation. *Psychophysiology* **45**, 602–607 (2008).

100. Mangin, E. N., Chen, J., Lin, J. & Li, N. Behavioral measurements of motor readiness in mice. 2023.02.03.527054 Preprint at https://doi.org/10.1101/2023.02.03.527054 (2023).

101. Yin, C. *et al.* Engaged decision-makers align spontaneous movements to stereotyped task demands. 2023.06.26.546404 Preprint at https://doi.org/10.1101/2023.06.26.546404 (2023).

102. Kim, T. H. *et al.* Long-Term Optical Access to an Estimated One Million Neurons in the Live Mouse Cortex. *Cell Reports* **17**, 3385–3394 (2016).

103. Jun, J. J. *et al.* Fully integrated silicon probes for high-density recording of neural activity. *Nature* **551**, 232–236 (2017).

104. Jun, J. J. *et al.* Real-time spike sorting platform for high-density extracellular probes with ground-truth validation and drift correction. *bioRxiv* 101030 (2017) doi:10.1101/101030.

105. Pachitariu, M., Sridhar, S. & Stringer, C. Solving the spike sorting problem with Kilosort. 2023.01.07.523036 Preprint at https://doi.org/10.1101/2023.01.07.523036 (2023).

106. Vincent, J. P. & Economo, M. N. Assessing cross-contamination in spike-sorted electrophysiology data. 2023.12.21.572882 Preprint at https://doi.org/10.1101/2023.12.21.572882 (2023).

107. Boumal, N., Mishra, B., Absil, P.-A. & Sepulchre, R. Manopt, a Matlab Toolbox for Optimization on Manifolds. *Journal of Machine Learning Research* **15**, 1455–1459 (2014).

108. Jiang, X., Saggar, H., Ryu, S. I., Shenoy, K. V. & Kao, J. C. Structure in Neural Activity during Observed and Executed Movements Is Shared at the Neural Population Level, Not in Single Neurons. *Cell Reports* **32**, 108006 (2020).

109. Aarts, E., Verhage, M., Veenvliet, J. V., Dolan, C. V. & van der Sluis, S. A solution to dependency: using multilevel analysis to accommodate nested data. *Nat Neurosci* **17**, 491–496 (2014).

1292   110. de Leeuw, J. & Meijer, E. *Handbook of Multilevel Analysis*. vols 401–433 (Springer, New York,
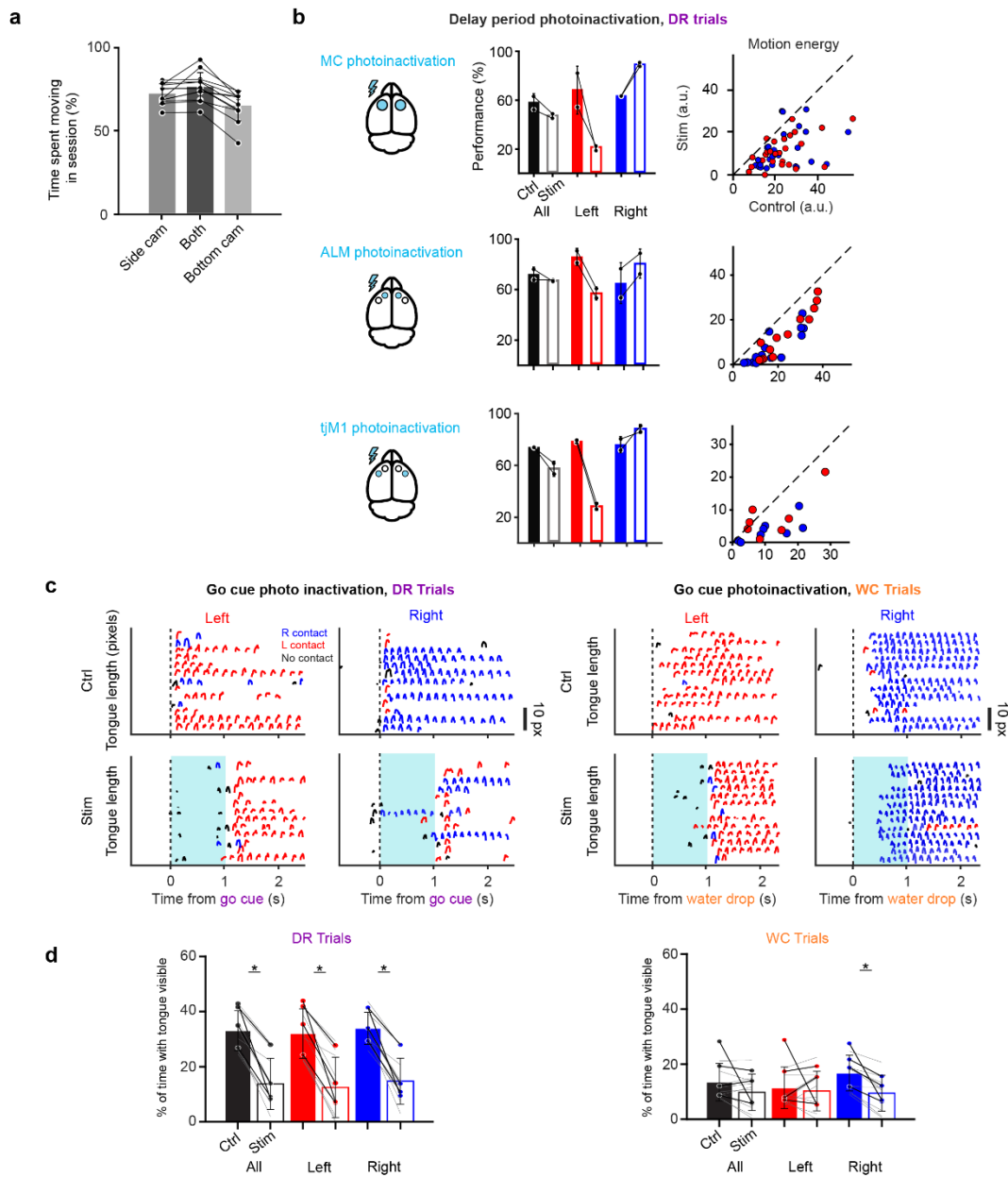
1293   2008).

1294

1295

1296

1297

1298

1299   **Extended Data**


1300

Extended Data Fig. 1 – Region-specific photoinactivation of ALM and tjM1. a. Percentage of time spent moving (see **Methods**) in a session determined by video recordings using the side view, bottom view, and both views. Points indicate each of the 12 randomly selected sessions used for this analysis. **b.** Effect of delay epoch photoinactivation on behavioral performance (*middle column*) and uninstructed

movements (*right column*) when photoinactivation was directed to the MC (ALM + tjM1; *top row*; same data as **Fig. 1g-i**, $n = 14$ sessions, 2 mice), the ALM (*middle row*, $n = 15$ sessions, 2 mice), and the tjM1 (*bottom*, $n = 9$ sessions, 2 mice). Photoinactivation of ALM and tjM1 led to similar behavioral impairment and reduction in uninstructed movements, with larger effects observed with MC (ALM + tjM1) photoinactivation. **c.** Tongue length during control and go cue photoinactivation trials for delayed-response (*left*) and water-cued (*right*) contexts. Blue traces indicate right lickport contacts, red traces indicate left contacts, and black traces indicate no contact. Vertical dashed line indicates go cue or water drop onset. Blue shaded region indicates photoinactivation period. **d.** Percentage of time with tongue visible during photoinactivation period for DR trials (*left*) and WC trials (*right*). Each colored point indicates mean value for an animal ($n = 4$ animals), individual animals are connected by black lines. Light gray lines denote individual sessions ($n = 10$ sessions). Bars are the mean across all sessions. Asterisks denote significant differences ($p < 0.05$) between control and photoinactivation trials (Percent reduction on all DR trials: $19 \pm 7\%$, mean $\pm$ s.d., $p = 1.6e-05$; DR left trials: $20 \pm 8\%$, $p = 3.0e-05$; DR right trials: $20 \pm 7\%$, $p = 1.6e-05$; All WC trials: $4 \pm 8\%$, p=0.154; WC left trials: $1\% \pm 9\%$, p=0.702; WC right trials: $7\% \pm 5\%$, p=0.002; paired *t*-test, n=10 sessions). Error bars indicate standard deviation across sessions. In WC trials, tongue protrusion was only significantly impaired on one trial type, while ability to successfully contact the lickport was impaired in all conditions (see **Fig. 1c**).
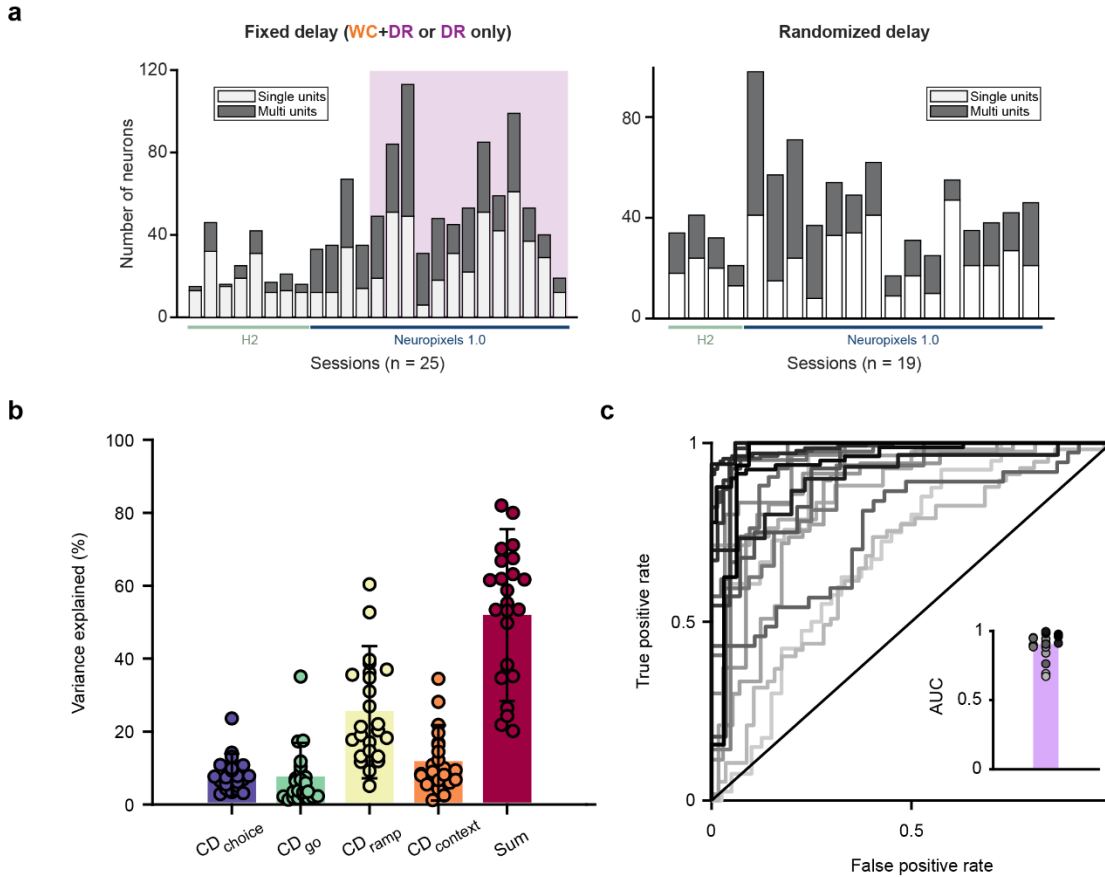

Extended Data Fig. 2 – Session-by-session statistics. a. Number of recorded single- and multi-units per session for the fixed delay task (*left*) or the randomized delay task (*right*). *Left*, Purple shaded region indicates sessions in which animals only performed presented with DR trials. Green and blue bars underneath plots indicate the probe type used for a given session **b.** Variance explained of trial-averaged neural activity by each coding direction. The coding directions were calculated using neural activity from individual sessions (n=25). Bar height represents the mean across sessions and error bars indicate standard deviation across sessions. **c.** Receiver operating curves (ROC) demonstrating choice decoding accuracy from delay epoch CD$_{choice}$ projections across all individual sessions (see **Methods**). Inset: area under the ROC curve (AUC). Bar height represents the mean across sessions and points indicate sessions.
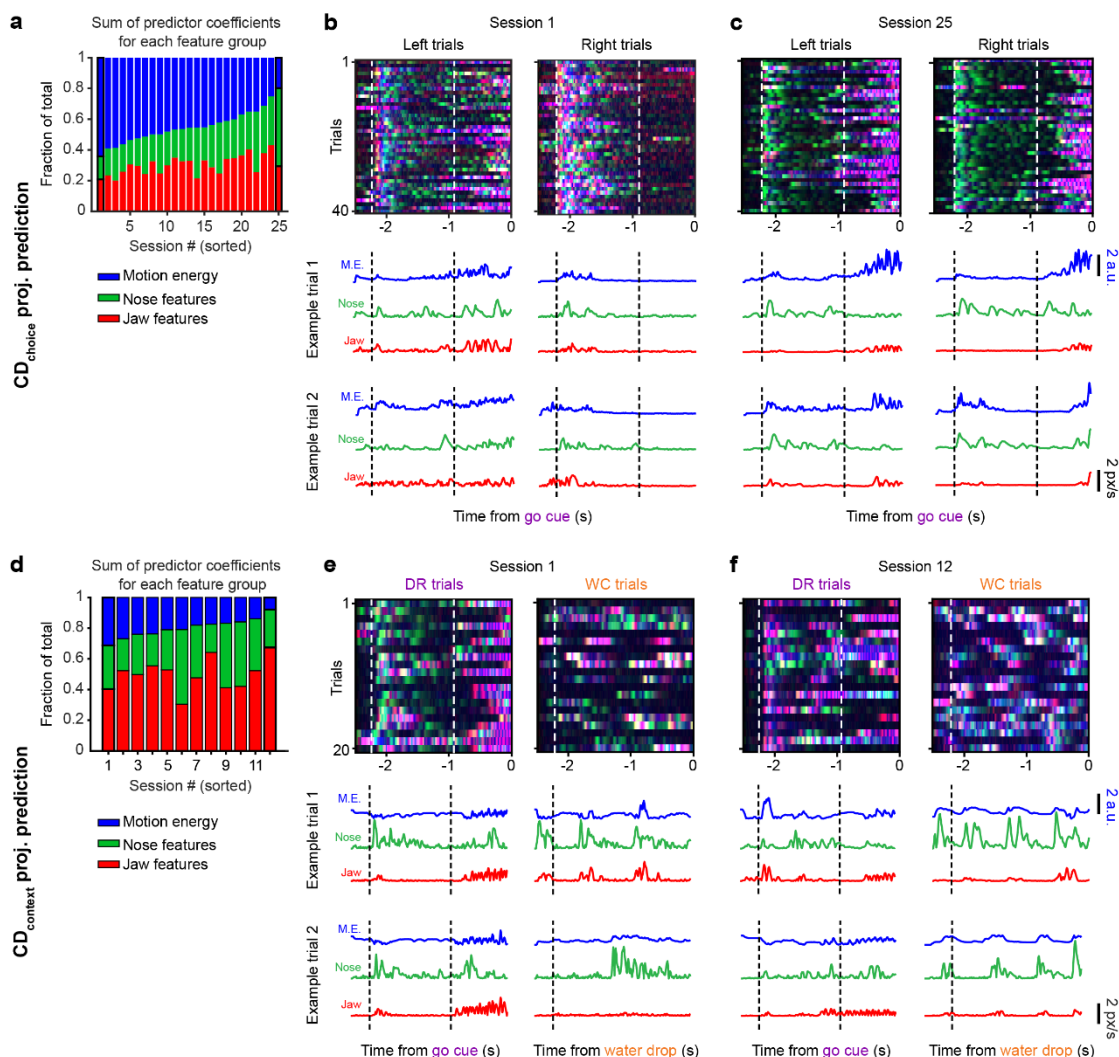
Extended Data Fig. 3 - Session-by-session variability in the relationship between kinematic features and putative cognitive dynamics.
a. Regression weights for each group of kinematic predictors of CD_{choice} projections, as a fraction of all predictor coefficients (see **Methods**). Sessions are sorted in descending order by motion energy fraction. Outlined bars indicate example sessions shown in (b) and (c). **b.** Example session where motion energy made up the largest fraction of regression weights for predicting CD_{choice} projections. *Top*, overlayed jaw/nose speed or motion energy for a subset trials. *Bottom*, two example trials of kinematic feature trajectories. **c.** Same as (b) but for an example session where jaw and nose features made up a larger fraction of regression weights. **d.** Same as (a) but for predicting $CD_{context}$ projections.
e, f. Same as (b) and (c) but for two example sessions with different regression weight fractions for predicting $CD_{context}$ projections.
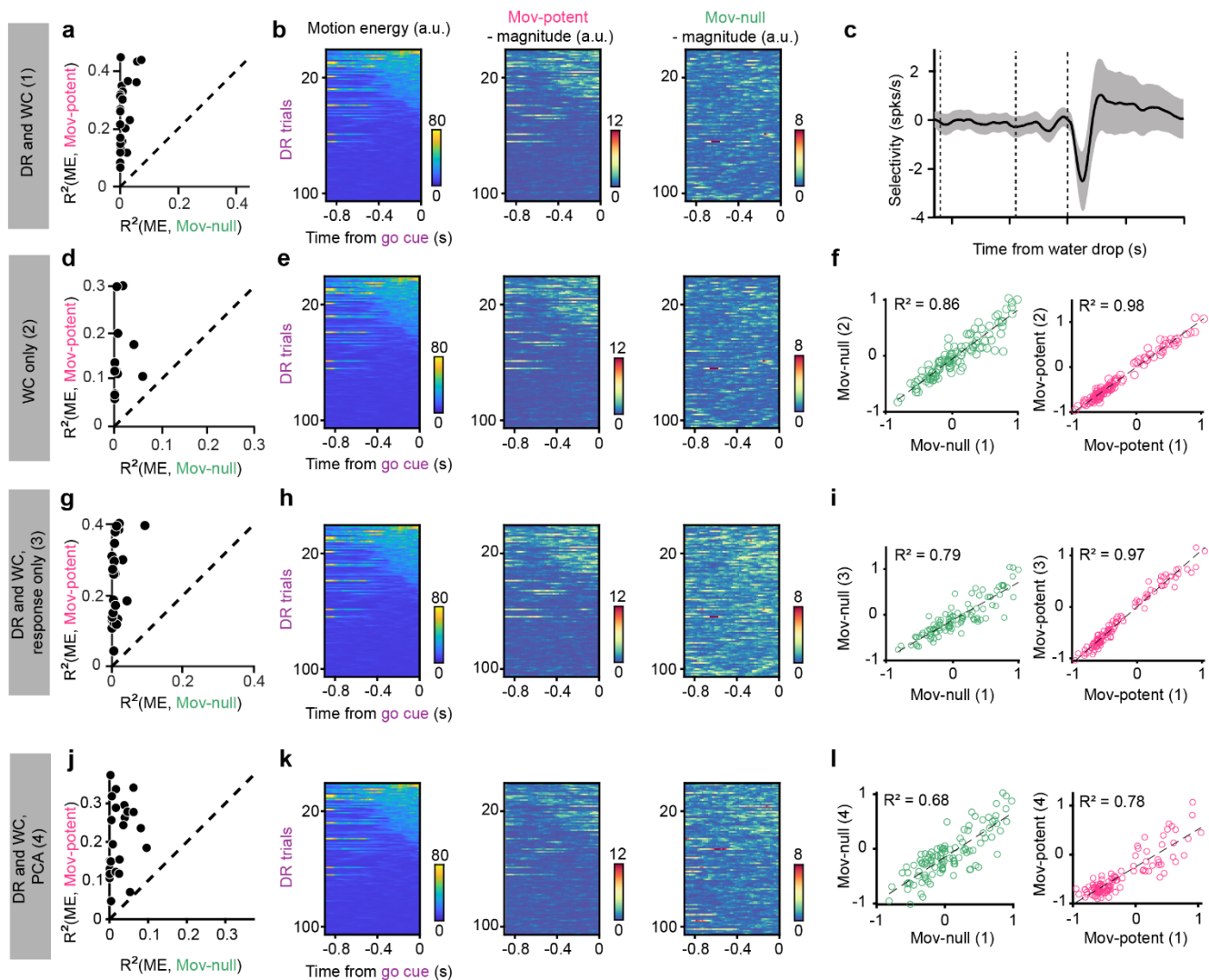
Extended Data Fig. 4 – Control analyses for subspace decomposition. a,b. Movement-null and movement-potent subspaces estimated as in **Fig. 5g-l** using DR and WC trials. **a.** Variance explained (R^2) of motion energy by the sum squared magnitude of activity in the movement-null and movement-potent subspaces on single trials. Each point is the mean across trials for a session. **b.** *Left*, motion energy on single trials for an example session. *Middle*, sum-squared magnitude of activity in the movement-potent subspace. *Right*, sum-squared magnitude of activity in the movement-null subspace. Trials sorted by average delay epoch motion energy. **c.** Selectivity (left vs. right) of the neural population during WC trials. Mean and 95% CI across sessions shown. **d,e.** Same as (a,b) but estimating movement-null and movement-potent subspaces using WC trials only. **f.** Normalized magnitude of activity in the movement-null subspace (*left*) movement-potent subspace (*right*) when estimated using DR and WC trials as in (a,b), versus when estimated using WC trials only as in (d,e). Circles are average activity per trial for an example session. **g,h.** Same as (a,b), but estimating movement-null and movement-potent subspaces using data restricted to the response epoch of DR and WC trials. **i.** Magnitude of activity in the movement-null subspace (*left*) or movement-potent subspace (*right*) when estimated using DR and WC trials as in (a,b) versus when estimated using data from only the response epoch of DR and WC trials as in (g,h). Circles are average activity per trial for an example session. **j,k.** Same as (a,b), but estimating the movement-null and movement-potent subspaces using a two-stage PCA approach (see **Methods**). This approach is conservative in avoiding the mis-assignment of cognitive dynamics that correlate in time with movement to the movement-potent subspace. **j.** Magnitude of activity in the movement-null subspace (*left*) or movement-potent subspace (*right*) when estimated using DR and WC trials as in (a,b) versus when estimated using the two-stage PCA approach as in (j,k). Circles are average activity per trial for an example session.
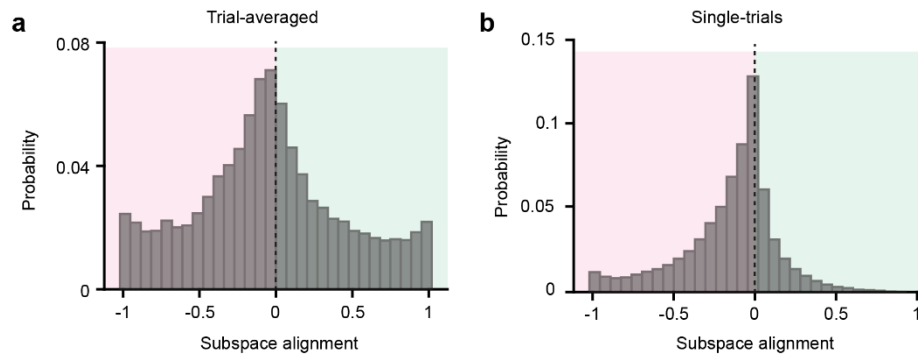
Extended Data Fig. 5 – Alignment of single-units to random subspaces. Random subspaces were constructed by independently and identically drawing from a normal distribution with zero mean and unit variance. Each random subspace was then biased towards the covariance structure of the actual data (see **Methods**). **a.** Null distributions of alignment indices for trial-averaged data. **b.** Null distributions of alignment indices for single-trial data. Null alignment distributions are skewed towards the movement-potent subspace due to the unbalanced variance between delay and response epochs (a) or between stationary and movement time points (b), reflecting the strong movement tuning of many units.
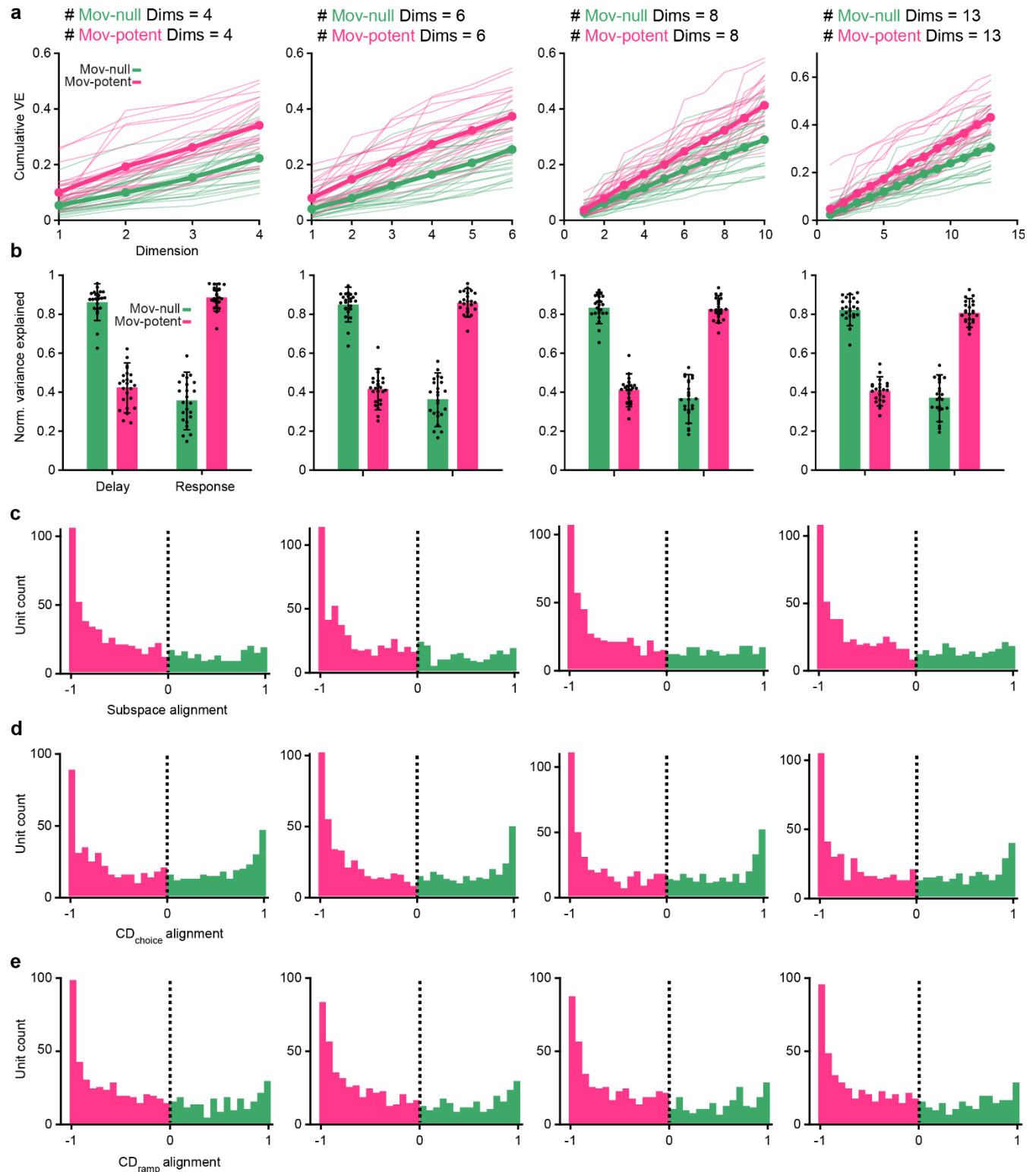
Extended Data Fig. 6 – Varying dimensionality of subspaces. Analyses were repeated while varying the dimensionality of movement-null and movement-potent subspaces. Each subspace was constrained to be 4 (*left*), 6 (*middle left*), 8 (*middle right*), or 13 dimensions (*right*). **A.** Cumulative variance explained of the neural activity by the activity in movement-null and movement-potent subspaces. Bold lines and points indicate mean across sessions. Thin lines represent single sessions **b.** Normalized variance explained of neural activity during the delay or response epoch by the activity in movement-null and movement-potent subspaces. Points indicate sessions, bar height indicates mean across sessions, and error bars indicate standard deviation across sessions (n=25 sessions). **c-e.** Subspace (**c**), CD_{choice} (**d**), and CD_{ramp} (**e**) alignment distributions when varying dimensionalities of each subspace.
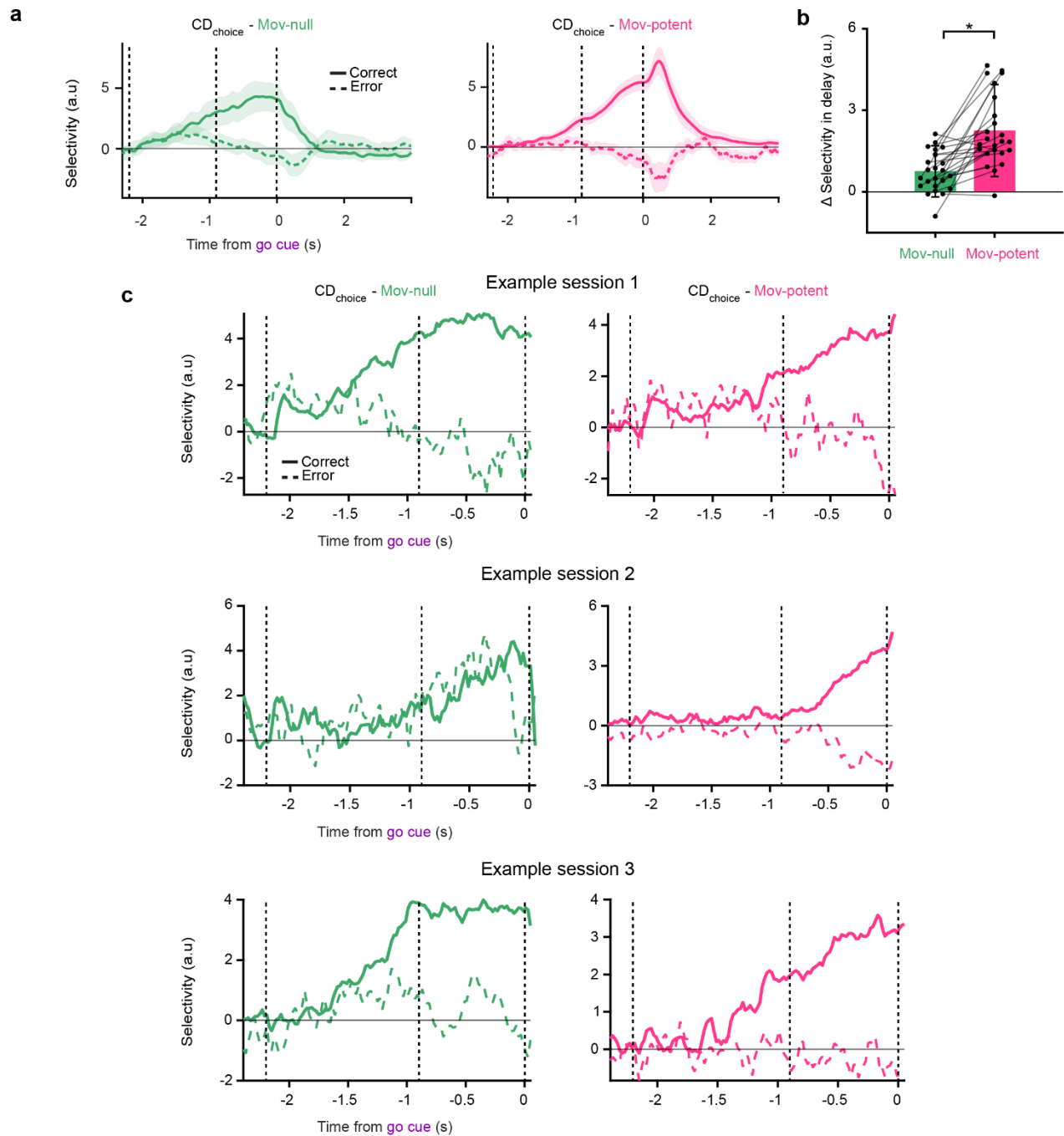
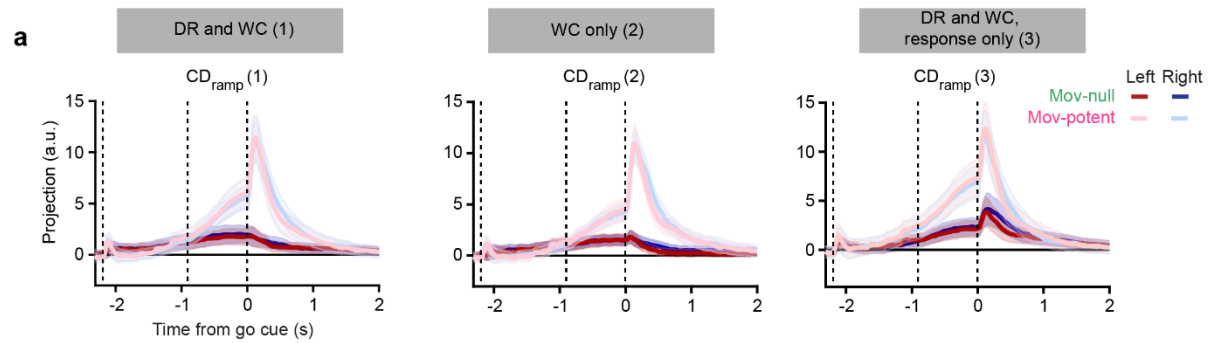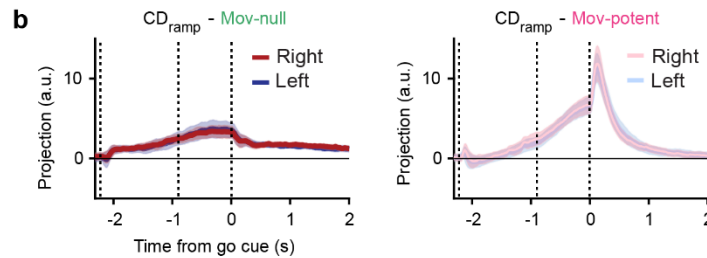**Extended Data Fig. 7 – Projections along movement-null and movement-potent components of CD_{choice}. a.** Same data as in **Fig. 7a** except all time in trial shown to highlight activity during the response epoch. Selectivity (projections onto CD_{choice} on lick-right trials minus projections on lick-left trials) of movement-null (*left*) and movement-potent (*right*) subspace activity. Mean and 5-95% CI of the bootstrap distribution for correct (*solid*) and error (*dashed*) trials shown. **b**. Change in selectivity between the last 100ms of the delay epoch and the last 100ms of the sample epoch in movement-null and movement-potent components of projections along CD_{choice} (Movement-potent: 2.25 ± 1.57, mean ± s.d., Movement-null: 0.76 ± 0.8, $p=1 \times 10^{-5}$, paired *t*-test, $n = 25$ sessions). Points indicate individual sessions, bar height indicates mean across sessions, and error bars indicate standard deviation across sessions. **c.** Three example sessions from three different mice depicting selectivity along CD_{choice} as in **Fig. 7a**. Solid lines denote the mean projection on correct trials and dashed lines denote the mean projection error trials.

Extended Data Fig. 8 – Within-subspace CD projections using variations on procedure to determine subspaces. a. Projections of movement-null and movement-potent subspace activity along CD_{ramp} for each of three analytical variations. Movement-null and movement-potent subspaces were identified using both DR and WC trials (*left*), WC trials only (*middle*), and the response epoch of DR and WC trials (*right*). Mean and 95% CI of bootstrap distribution shown.. **b.** Projections along movement-null (*left*) and movement-potent (*right*) components of CD_{ramp} when determined from activity within each subspace individually, rather than from the full neural population. Mean and 95% CI of bootstrap distribution shown.
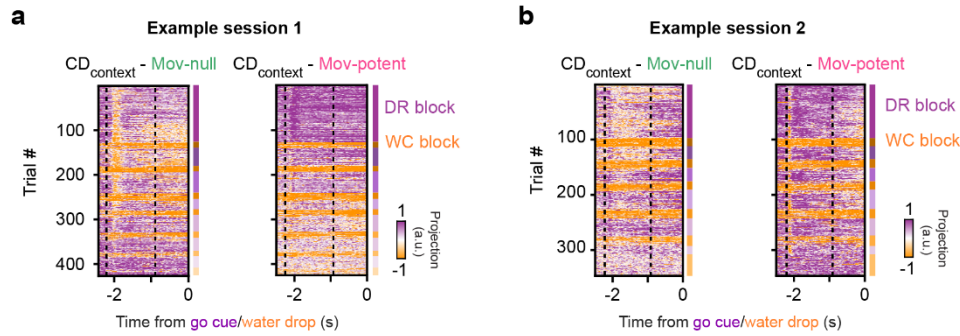
Extended Data Fig. 9 – Encoding of context in both the null and potent subspaces tracks block-wise task structure. a. Heatmap of single-trial projections of null and potent subspace activity along $CD_{context}$ for an example session. The chronological DR or WC block within the session is denoted by differently shaded purple and orange rectangles, respectively, on the right of each plot. **b.** Same as (a) but for another example session, from a different animal.
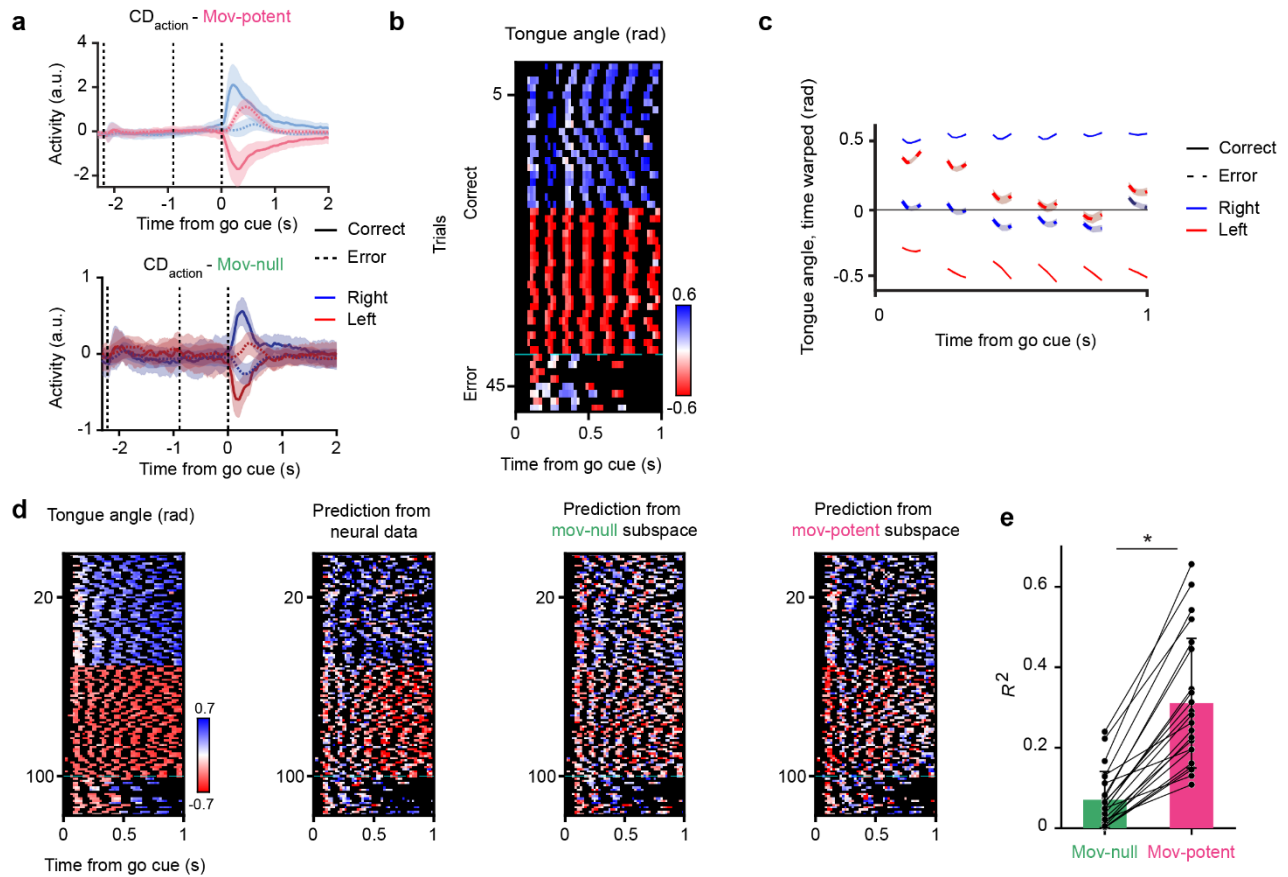
Extended Data Fig. 10 – Relationship between tongue angle and neural activity in the movement-null and movement-potent subspaces. a. Projections along movement-potent (*top*) and movement-null (*bottom*) components of CD_{action}. Correct trials shown in solid lines and error trials shown in dashed lines. **b.** Tongue angle for an example session for correct and error trials Black values indicate tongue not visible. **c.** Tongue angle on correct and error right and left trials. Tongue angle was linearly time warped to allow for averaging over trials and sessions. Mean and s.e.m. across sessions shown. **d.** Tongue angle (*left*) and predictions from the full population neural activity (*middle left*), null subspace activity (*middle right*), and potent subspace activity (*right*) for an example session. **e.** Variance explained (R^2) of tongue angle by prediction from movement-null (*green*) and movement-potent (*pink*) subspaces. Asterisks denote significant differences between predictions from null and potent subspaces ($p=2 \times 10^{-8}$, paired t-test, n=25 sessions).

Supplementary Movie 1 – Uninstructed movements vary in their identity and timing. Example trials in which uninstructed movements vary in their identity (across rows) and timing (across columns). Traces represent the y-position of the feature within the video frame. All example trials taken from the same mouse and session.